



저작자표시-비영리-동일조건변경허락 2.0 대한민국

이용자는 아래의 조건을 따르는 경우에 한하여 자유롭게

- 이 저작물을 복제, 배포, 전송, 전시, 공연 및 방송할 수 있습니다.
- 이차적 저작물을 작성할 수 있습니다.

다음과 같은 조건을 따라야 합니다:



저작자표시. 귀하는 원저작자를 표시하여야 합니다.



비영리. 귀하는 이 저작물을 영리 목적으로 이용할 수 없습니다.



동일조건변경허락. 귀하가 이 저작물을 개작, 변형 또는 가공했을 경우에는, 이 저작물과 동일한 이용허락조건하에서만 배포할 수 있습니다.

- 귀하는, 이 저작물의 재이용이나 배포의 경우, 이 저작물에 적용된 이용허락조건을 명확하게 나타내어야 합니다.
- 저작권자로부터 별도의 허가를 받으면 이러한 조건들은 적용되지 않습니다.

저작권법에 따른 이용자의 권리는 위의 내용에 의하여 영향을 받지 않습니다.

이것은 [이용허락규약\(Legal Code\)](#)을 이해하기 쉽게 요약한 것입니다.

[Disclaimer](#)

의학박사 학위논문

Identification of viable cell
populations in docetaxel-treated
breast tumors using ferritin-
based magnetic resonance imaging

유방암의 도세탁셀 치료 후 페리틴
자기공명영상을 이용한 생존 세포 집단의 동정

2014 년 02 월

서울대학교 대학원

의과학과 박사과정

최 윤 석

A thesis of the degree of doctor of philosophy

Identification of viable cell
populations in docetaxel-treated
breast tumors using ferritin-
based magnetic resonance imaging

February 2014

The Department of Biomedical Sciences,
Seoul National University
College of Medicine
YoonSeok Choi

Identification of viable cell
populations in docetaxel-treated
breast tumors using ferritin-
based magnetic resonance imaging

by
YoonSeok Choi

A thesis submitted to the Department of
Biomedical Sciences in partial fulfillment of the
requirements for the Degree of Doctor of
Philosophy in Biomedical Sciences at Seoul
National University College of Medicine

February 2014

Approved by Thesis Committee:

Professor _____ Chairman

Professor _____ Vice chairman

Professor _____

Professor _____

Professor _____

ABSTRACT

Introduction: Cancer stem cells (CSCs) are highly tumorigenic and are responsible for tumor progression and chemoresistance. Noninvasive imaging methods for the visualization of CSC populations within tumors in vivo will have a considerable impact on the development of new CSC-targeting therapeutics.

Methods: In this study, human breast cancer stem cells (BCSCs) transduced with dual reporter genes (human ferritin heavy chain [FTH] and enhanced green fluorescence protein [EGFP]) were transplanted into NOD/SCID mice to allow noninvasive tracking and quantification of BCSC-derived populations during docetaxel treatment.

Results: No changes in the properties of the BCSCs were observed due to ferritin overexpression. Magnetic resonance imaging (MRI) revealed significantly different signal intensities (R_2^* values) between BCSCs and FTH-BCSCs in vitro and in vivo. In addition, distinct populations of pixels with high R_2^* values were detected in docetaxel-treated FTH-BCSC tumors compared with control tumors, even before the tumor sizes changed. Histological analysis revealed that areas showing high R_2^* values in docetaxel-treated FTH-BCSC tumors by MRI contained EGFP+/FTH+ viable cell

populations with high percentages of CD44+/CD24- cells.

Conclusions: These findings suggest that ferritin-based MRI, which provides high spatial resolution and tissue contrast, can be used as a reliable method to identify viable cell populations derived from BCSCs after chemotherapy and may serve as a new tool to monitor the efficacy of CSC-targeting therapies in vivo.

Keywords: Human breast cancer stem cell, Ferritin, Chemotherapy, Reporter gene, Magnetic resonance imaging

Student number: 2009-30615

CONTENTS

Abstract	i
Contents.....	iii
List of tables and figures.....	iv
List of abbreviations	vii
General introduction	1
Chapter 1	6
Establishment of ferritin overexpressing breast cancer stem cells	
Introduction.....	7
Material and methods.....	9
Results	16
Discussion.....	29
Chapter 2	31
Noninvasive identification of viable cell populations in docetaxel-treated breast tumors	
Introduction.....	32
Material and methods.....	34
Results	41
Discussion.....	70
References.....	74
Abstract in Korean	79

LIST OF TABLES AND FIGURES

Chapter 1

Figure 1-1. Biological properties of human BCSCs	20
Figure 1-2. Aldehyde dehydrogenase activity of BCSCs	21
Figure 1-3. Lentiviral vector of myc-tagged heavy chain subunit of ferritin (myc-FTH) and EGFP	22
Figure 1-4. Establishment of FTH-BCSCs	23
Figure 1-5. Biological characteristics of FTH-BCSCs	24
Figure 1-6. Mammosphere forming ability assay	25
Figure 1-7. Measurement of cellular iron levels	26
Figure 1-8. Cell growth analysis and the 7-AAD assay with iron supplementation	27
Figure 1-9. MRI phantom images and analysis	28

Chapter 2

Table 2-1. Evaluation of the incidence of tumors in NOD/SCID mice implanted with different numbers of BCSCs and FTH-BCSCs	48
Table 2-2. Mean R_2^* values of control (BCSC and FTH-BCSC) and docetaxel-treated (BCSC Doc and FTH-BCSC Doc) xenograft tumors	60
Table 2-3. R_2^* threshold values of docetaxel-untreated	

(BCSC and FTH-BCSC) and docetaxel-treated (BCSC Doc and FTH-BCSC Doc) xenograft tumors at day 0, day 5 and day 14	61
Figure 2-1. Comparison of tumor-forming abilities and fluorescence imaging of BCSCs and FTH-BCSC-derived tumors.....	49
Figure 2-2. MRI images of xenograft tumors.....	51
Figure 2-3. Growth rates of BCSC, FTH-BCSC, BCSC Doc and FTH-BCSC Doc tumors.....	52
Figure 2-4. Slice-by-slice analysis of R_2^* values in the xenograft tumors	54
Figure 2-5. Volumetric MRI images of control (BCSC and FTH-BCSC) and docetaxel-treated (BCSC Doc and FTH-BCSC Doc) xenograft tumors	56
Figure 2-6. Distribution of R_2^* values in control (BCSC and FTH-BCSC) and docetaxel-treated (BCSC Doc and FTH-BCSC Doc) xenograft tumors	57
Figure 2-7. Analysis of pixels over threshold (mean + 3 SDs).....	59
Figure 2-8. Histological analysis of the peripheral and central portions of control and docetaxel-treated xenograft tumors.....	62
Figure 2-9. Immunostaining of EGFP and myc-FTH in FTH-BCSC and FTH-BCSC Doc tumors	64
Figure 2-10. In vitro cytotoxicity test in BCSCs and FTH-	

BCSCs with docetaxel treatment	65
Figure 2-11. Immunohistochemical analysis of the peripheral and central portions of FTH-BCSC and docetaxel-treated FTH-BCSC Doc xenograft tumors.....	67
Figure 2-12. Analysis of tumor cell proliferation.....	69

LIST OF ABBREVIATIONS

Cancer stem cell: CSC

Breast cancer stem cell: BCSC

Ferritin heavy chain: FTH

Ferritin overexpressing breast cancer stem cell: FTH-BCSC

Enhanced green fluorescence protein: EGFP

Cluster of differentiation: CD

Positron emission tomography: PET

Magnetic resonance imaging: MRI

Superparamagnetic iron oxide: SPIO

Nonobese diabetic/severe combined immunodeficient: NOD/SCID

Nuclear magnetic resonance: NMR

Cytomegalovirus promoter: CMV promoter

Phosphoglycerate kinase promoter: PGK promote

Phosphate buffered saline: PBS

Phytoerythrin: PE

Allophycocyanin: APC

Aldehyde dehydrogenase: ALDH

BodipyTM-aminoacetaldehyde: BAAA

Diethylaminovenzaldehyde: DEAB

Fluorescence-activated cell sorting: FACS

SDS-polyacrylamide gel electrophoresis: SDS-PAGE

7-amino-actinomycin D: 7-AAD

Ferric ammonium citrate: FAC

Time of repetition: TR

Time of echo: TE

Field of view: FOV

Regions of interest: ROI

Standard deviation: SD

Analysis of variance: ANOVA

3-(4,5-Dimethylthiazol-2-yl)-2,5-Diphenyltetrazolium Bromide: MTT

Hematoxylin and eosin staining: H&E

Phospho histone: PH3

GENERAL INTRODUCTION

Since the first identification of breast cancer stem cells (BCSCs) from human tumor samples using CD44⁺/CD24⁻ markers by Al-Hajj et al., the role of BCSCs in tumor progression and therapeutic resistance has been actively investigated to develop better anti-cancer treatment strategies (1, 2). In breast cancer patients, administration of chemotherapy or radiation therapy increases the fraction of CD44⁺/CD24⁻ tumor cells and augments mammosphere formation in vitro and tumorigenicity in xenotransplantation models (3, 4). The presence of BCSC markers or gene expression signatures correlates with poor prognosis in clinical tumor samples (5, 6). The therapeutic resistance of BCSCs is associated with alterations in self-renewal and cell fate signaling pathways, including Notch, Wnt, Hedgehog, and HER-2 (2). New therapeutic regimens using single agents or a combination of various drugs that target BCSCs are now under preclinical or clinical trials. Monitoring the efficacy of cancer stem cell (CSC) therapeutics in vivo, however, is challenging because the conventional method of measuring tumor size is inadequate as an endpoint (7). In vivo identification of BCSCs using cellular imaging techniques will be extremely useful for this purpose because the efficacy of treatment

depends more on the fraction of viable cancer cells in the tumor (8, 9).

In vivo imaging methods, including intravital microscopy, fluorescent imaging, luciferase imaging, positron emission tomography (PET), and magnetic resonance imaging (MRI), have been used to track cancer cells and monitor treatment response (10–15). However, there have only been a few reports of in vivo imaging of CSCs in different types of tumors (16, 17). Snyder et al. analyzed CSCs using quantum dot–conjugated antibodies against CD44v6 and CD24 in tumors and suggested the possibility of applying this approach to BCSC imaging (12). Vlashi et al. demonstrated reduced 26S proteasome activity in CSCs originating from glioma cells and monitored these CSCs in vivo using a fluorescent protein (ZsGreen) fused to ornithine decarboxylase, which is a target of the 26S proteasome (13). Liu et al. longitudinally monitored CSCs derived from breast cancer patients in an orthotopic xenograft mouse model using ubiquitin promoter–driven luciferase and showed the role of BCSCs in metastasis with imaging techniques (14). Recently, Yoshii et al. showed that in a mouse colon carcinoma model, Cu-64–ATSM, a PET imaging agent, localizes preferentially in tumor regions with a high density of

CD133+ cells with CSC characteristics (15). However, in vivo imaging of BCSCs using MRI or PET has not been reported to date. MRI can provide tomographic or volumetric imaging of internal organs at high anatomical resolutions and soft tissue contrast without using ionizing radiation, which is not possible with other imaging modalities. Clinically, MRI is routinely used to identify and localize tumors before surgery and to monitor the response to treatment in breast cancer (18).

There are two approaches to track and image cells of interest in vivo with MRI. The first method uses a contrast agent as a labeling or targeting agent. To date, superparamagnetic iron oxide (SPIO) nanoparticles, due to their high relaxivity, have been the most widely used contrast agents for tracking and imaging diverse cells (19, 20). With surface modification of SPIO nanoparticles, cells of interest can be targeted by an antibody, peptide, or nucleotide conjugation (21). The presence of SPIO nanoparticles in the magnetic field leads to low signal intensities in T_2 or T_2^* sensitive images. However, this method does not enable the long-term imaging of the cells of interest because the contrast agents become diluted as the cells divide, and the SPIO nanoparticle signals can accumulate in sites within tumors, where the cells are not viable (9).

The use of the MRI reporter gene ferritin can overcome these limitations (22–26). The overexpression of ferritin enables cells to uptake more iron, and this reporter produces low signal intensities in MRI. As MRI reporters are stably expressed, even during cell division, they can be used for studying dynamic processes, e.g., the migration and invasion of cells of interest over an extended period of time and can also be useful for providing temporal and spatial information for anti-cancer treatment effects on a specific cell population. The number of cancer cells or level of tumor burden in deep tissues can be quantified by calculating R_2^* ($=1/T_2^*$) values from T_2^* mapping of MRI images (27, 28). In addition, the introduction of optical reporter genes, such as EGFP or luciferase, and ferritin together allows for the analysis of cancer cells isolated from tumors in molecular biology and histology experiments.

In the present study, BCSCs isolated from human breast cancer specimens were transduced with MRI (human ferritin heavy chain, FTH) and fluorescence (enhanced green fluorescence protein, EGFP) dual reporter genes and transplanted into nonobese diabetic/severe combined immunodeficient (NOD/SCID) mice to noninvasively track BCSC-derived populations during tumor growth

and monitor tumor responses after chemotherapy. An MRI evaluation of ferritin-overexpressing BCSCs (FTH-BCSCs) was performed, and the tumor response to chemotherapy was determined by quantification of the R_2^* values for entire tumors. In addition, viable cells were identified and localized by volumetric MRI, and BCSC characteristics were investigated by histological analysis.

CHAPTER 1

Establishment of ferritin overexpressing breast
cancer stem cells

INTRODUCTION

BCSCs have been observed to possess the ability to self-renew, proliferate and maintain the tumor. They are also refractory to therapy and acquire resistance to chemotherapy. Many researchers pointed out the importance of cancer stem cell specific therapies and development of non-invasive imaging technique because the development of BCSC imaging will facilitate the study and knowledge of BCSCs and provide additional information for example, the therapeutic response and the behavior of BCSCs under specific environment (8). Still there are only few studies that can show the BCSCs behavior and response to anti-cancer drug non-invasively with MRI.

Ferritin is the endogenous iron storage protein and consists of 24 subunits of light and heavy polypeptide chains (29). Biological functions of ferritin are not restricted to iron storage but also protect the cells against the free radicals and reactive oxygen species generated by free iron ion. In 1996, ferritin was first proposed as a magnetic resonance (MR) reporter gene with nuclear magnetic resonance (NMR) study by Gottesfeld Z and Neeman M (30). Despite the need for high Tesla MR modality, various applications of ferritin as a feasible and reproducible MR reporter

gene have been performed for MRI of cells and tissues. Xenografted cancer and stem cells stably expressing ferritin were visualized by MRI (22, 31) and adenoviral delivery of ferritin had succeeded to visualize the endogenous brain cells of mice (23). In addition, conditional transgenic mice that bearing human ferritin showed successful MRI of specific tissues overexpressing ferritin (32). Many groups are still trying to monitor cancer cells and to evaluate the therapeutic efficacy of cancer by using MRI based on ferritin.

In the present study, ferritin was used as a MR reporter gene and showed the feasibility of MR imaging of BCSCs without any biological property changes.

MATERIALS AND METHODS

1. Ethics Statement

All of the procedures were performed following approval by the Institutional Review Board (IRB) at Seoul National University Hospital. IRB approval number is H-0502-142-007. The individual in this manuscript has given written informed consent with the Declaration of Helsinki to publish these case details.

2. Culture of BCSCs

In this study, BCSCs were kindly gifted from Dr. Noh group in Seoul National University. The BCSCs were incubated with DMEM mixed 3:1 with Ham's F12 medium (Invitrogen) supplemented with basic fibroblast growth factor (10 ng/ml; Millipore), epidermal growth factor (20 ng/ml; Invitrogen), leukemia inhibitory factor (10 ng/ml; Millipore), B27 supplement (Invitrogen) and antibiotic-antimycotic solution (Invitrogen) for mammosphere culture.

3. Establishment of FTH-BCSCs by transduction of a lentivirus expressing myc-tagged FTH

To establish the FTH-BCSCs, a lentivirus expressing myc-tagged FTH (myc-FTH) and EGFP driven by the cytomegalovirus

(CMV) and phosphoglycerate kinase (PGK) promoters, respectively, was introduced into cells by incubating the cells with 10^6 – 10^7 transduction units/ml for 6–10 hours in the presence of 8 μ g/ml polybrene. After three days of transduction, cells expressing EGFP were sorted using a FACS–Aria, expanded and used in all experiments.

4. Analysis of surface markers on BCSCs and FTH–BCSCs

To analyze cell surface markers, 5×10^5 BCSCs and FTH–BCSCs were dissociated from mammospheres and washed two times with phosphate buffered saline (PBS) containing 1% BSA. The cells were then incubated with anti–huCD44–phytoerythrin (PE), anti–huCD24–PE, anti–huCD90–allophycocyanin (APC), α –huCD105–PE, α –huCD49f–PE and α –huEpCAM–PE antibodies (BD Biosciences) for one hour at 37° C. Cell–associated fluorescence was measured using a FACS–Calibur flow cytometer (BD Biosciences). The data were analyzed using CellQuest software (BD Biosciences).

5. ALDEFLUOR assay

Aldehyde dehydrogenase (ALDH) activity of cells was measured using ALDEFLUOR assay kit (StemCell Technologies). As negative control, 100 mmol/l of diethylaminovenzaldehyde (DEAB) was used. In experimental group, 1 mol/l of ALDH substrate, BodipyTM-aminoacetaldehyde (BAAA), was used for 5 x10⁶ cells and incubated 2 hours at 37 ° C.

6. Western blot analysis

Cells were lysed in RIPA buffer with 1 mM phenylmethylsulfonyl fluoride and a protease inhibitor cocktail (Sigma–Aldrich Chemical Co.). The protein lysates were resolved by SDS–polyacrylamide gel electrophoresis (SDS–PAGE) for four hours at room temperature and were transferred to nitrocellulose membranes for two hours at 4° C. After blocking, the membranes were incubated with anti–FTH (Santa Cruz Biotechnology) and anti–EGFP (Santa Cruz Biotechnology) antibodies overnight at 4° C followed by incubation with HRP–conjugated antibodies (Santa Cruz Biotechnology) at room temperature for 30 minutes. Blots were visualized using enhanced chemiluminescence reagents (Amersham Biosciences).

7. Immunocytochemistry of mammospheres

Mammospheres were fixed in 4% paraformaldehyde in PBS. For the detection of myc-FTH expression, fixed mammospheres were incubated with anti-c-myc antibody (Santa Cruz Biotechnology) overnight at 4° C followed by incubation with the Alexa Fluor 594-conjugated anti-mouse IgG antibody (Invitrogen) at room temperature for one hour. Hoechst 33342 (Invitrogen) was used to visualize cell nuclei. Images were scanned and analyzed with a confocal laser microscope (LSM 5 META, Carl Zeiss).

8. Mammosphere assay

To compare the mammosphere-forming abilities of the BCSCs and FTH-BCSCs, dissociated cells from BCSC and FTH-BCSC mammospheres were seeded in 96-well plates at a density of 100 cells/well and incubated for four days. The average number of mammospheres was calculated by counting the number of mammospheres in a well.

9. Cell growth and viability with iron supplementation

To evaluate the growth and viability of the cells under different iron supply conditions, the trypan blue exclusion assay and flow

cytometric analysis with 7-amino-actinomycin D (7-AAD) (BD Pharmingen) were performed. For the cell growth assays, 3×10^4 BCSCs or FTH-BCSCs were initially seeded in 12-well plates supplemented with FAC (up to $50 \mu\text{M}$), and the average number of cells was calculated on days 2, 4, 6 and 8. For the cell viability assays, BCSCs and FTH-BCSCs were grown in medium supplemented with increasing amounts of FAC for five days. Next, both cell types were collected, incubated with 7-AAD for 5–10 minutes at 37°C and analyzed by flow cytometry.

10. Measurement of iron loading

BCSCs or FTH-BCSCs (2×10^4) were placed in 12-well Petri dishes, and 0 to $50 \mu\text{M}$ ferric ammonium citrate (FAC; Sigma-Aldrich Chemical Co.) was added to the culture medium for 4 days. Harvested cells were counted and subsequently lysed with 6 N HCl to extract total iron. The amount of total iron was determined using a total iron reagent kit (Pointe Scientific), and the average iron amount in a cell was calculated by dividing the total mean iron by the cell number.

11. MRI examination

MRI study was performed on a 9.4-T BrukerBiospec scanner (BrukerBiospin). A transmit-only volume coil and a four-channel surface coil (BrukerBiospin) were used for excitation and signal reception, respectively. For in vitro MRI, phantoms containing 2×10^6 BCSCs and FTH-BCSCs, which were treated with or without 25 μ M FAC for 4 days, were prepared. A multi-slice, multi-echo gradient echo sequence was used for in vitro T_2^* mapping. The parameters were as follows: matrix size = 256 x 256, repetition time (TR) = 5000 ms, slice thickness = 1 mm (no gap), flip angle = 90° , field of view (FOV) = 25 x 25 mm², TE = 3.1-43.1 ms with a step size of 10 ms (five-point T_2^* mapping), 13 slices and 4 signal averages.

12. MRI data analysis

All data post-processing was performed with Matlab (Mathworks Inc.). For phantom data, regions of interest (ROIs) were defined in each individual, imaging slices were acquired at the shortest TE and T_2^* maps of the ROIs were later estimated by pixel-by-pixel analyses across the multi-point MRI images, assuming single exponential decay. After performing the R_2^* analyses, R_2^* color

maps were merged with the anatomical images acquired at the shortest TE.

13. Statistical analysis

All data are presented as the mean \pm SD for at least three independent experiments. The mean values of the data were statistically evaluated using ANOVA followed by an unpaired t-test. For all tests, P-values less than 0.05 or 0.01 were considered to be statistically significant.

RESULTS

Isolated cells from breast cancer patient showed BCSC characteristics and the high ALDH activity

BCSCs from a breast cancer patient with a CD44+/CD24- phenotype were isolated and maintained using mammosphere culture media. Cell surface markers CD44/CD24 were analyzed to confirm the human BCSCs properties. Also, mesenchymal lineage markers (CD90 and CD105) and epithelial cell marker (EpCAM) were analyzed to identify the origin of BCSCs. High levels of CD44, low or negative levels of CD24 and EpCAM and high level of CD90 and CD105 were observed. In addition, well-known breast cancer marker CD49f was highly expressed (Figure 1-1). Up to 26.1% of BCSCs were shifted with aldefluor reagent (BAAA) compared to DEAB (an inhibitor of ALDH) treated group (Figure 1-2) and confirmed that BCSCs were positive for ALDH activity.

The transduction of FTH and EGFP does not alter BCSC characteristics

To establish ferritin-overexpressing BCSCs, genes for myc-FTH and EGFP plasmid vector (Figure 1-3) was transduced into cells with a lentiviral vector, and fluorescence-activated cell

sorting (FACS) was used to collect the cells that expressed both myc-FTH and EGFP. Immunofluorescence staining and western blot analysis revealed the expression of myc-FTH and EGFP in FTH-BCSCs (Figure 1-4A and B).

To determine whether the FTH-BCSCs retained their BCSC properties compared to control BCSCs, cell surface markers of breast cancer stem cell markers, mesenchymal lineage markers were investigated. The levels of BCSC markers (CD44+/CD24-) did not change in the FTH-BCSCs. The human mammary stem cell marker CD49f was highly expressed in both BCSCs and FTH-BCSCs (33). High levels of CD90 and CD105 and low levels of EpCAM were observed, and the levels of all of these surface markers did not differ between the FTH-BCSCs and BCSCs (Figure 1-5).

In addition, the mammosphere-forming abilities of the BCSCs and FTH-BCSCs were compared. Four days after single-cell dissociation, BCSCs and FTH-BCSCs generated mammospheres, and no substantial differences were observed in the average numbers of mammospheres (Figure 1-6).

Taken together, these findings demonstrate that the FTH-BCSCs retained the biological properties of the parent BCSCs.

FTH-BCSCs showed increased iron loading abilities without any cytotoxic effects on cells

Because FTH-BCSCs overexpress ferritin, an intracellular iron storage protein, we compared the intracellular iron loading abilities between BCSCs and FTH-BCSCs. After 4 day- treatment with increasing concentration of FAC (0, 10, 25 and 50 μ M), the cellular iron levels of both cells were measured. Iron-loading abilities were investigated with the addition of up to 50 μ M of FAC to both the FTH-BCSCs and BCSCs. The cellular iron levels of both groups increased in a dose-dependent manner, but the FTH-BCSCs had significantly higher iron levels compared with the BCSCs (Figure 1-7; $P < 0.05$ in 25 and 50 μ M of FAC).

The effects of iron overload on the growth and viability of the BCSCs and FTH-BCSCs were also investigated. The growth rates of the BCSCs and FTH-BCSCs were not affected by treatment with FAC (Figure 1-8A) and cytotoxicity was not observed in either group following treatment with 25 μ M FAC (Figure 1-8B), which is regarded as the physiological iron concentration in mouse serum (250-350 μ g/dl) (31).

FTH-BCSCs exhibit a significant increase in R_2^* values in MRI compared to BCSCs

To analyze the R_2^* values of the BCSCs and FTH-BCSCs, cells were incubated with or without 25 μ M FAC, and MRI images of cell phantoms were obtained (Figure 1-9A). The mean R_2^* values of the FTH-BCSCs ($97.85 \pm 0.51 \text{s}^{-1}$) treated with 25 μ M FAC were significantly higher than those of the BCSCs ($90.72 \pm 0.21 \text{s}^{-1}$). However, the mean R_2^* values of the FTH-BCSCs and BCSCs in the absence of FAC were not different (Figure 1-9B). With the results of enhanced ability for iron storage of FTH-BCSCs, in vitro phantom data suggested the feasibility of FTH-BCSC as a tool for distinguishing the ferritin overexpressing BCSCs from native BCSCs in MR images.

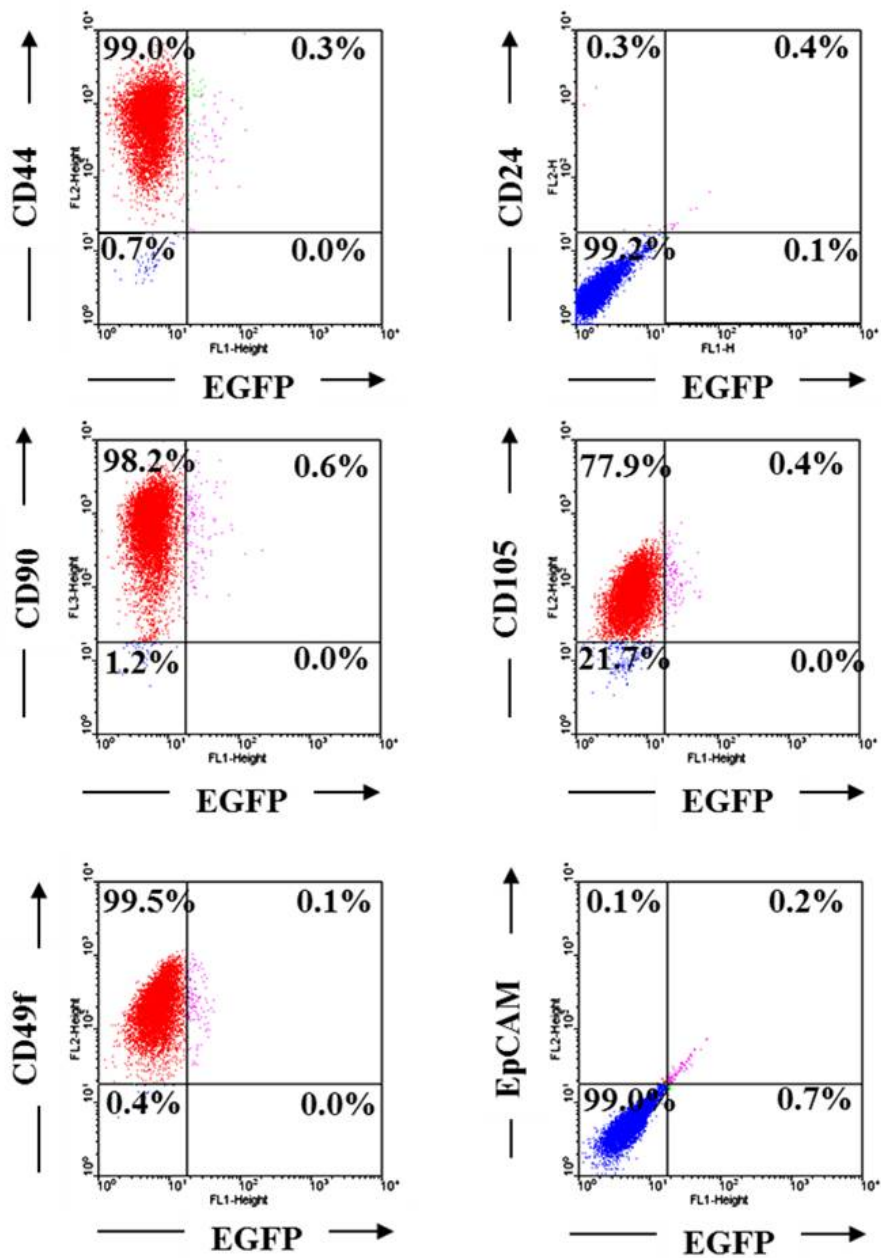


Figure 1-1. Biological properties of human BCSCs.

BCSC markers (CD44⁺/CD24⁻/CD49f^{high}), mesenchymal lineage markers (CD90^{high}/CD105^{high}) and epithelial lineage marker (EpCAM^{low}) in BCSCs were analyzed by flow cytometry.

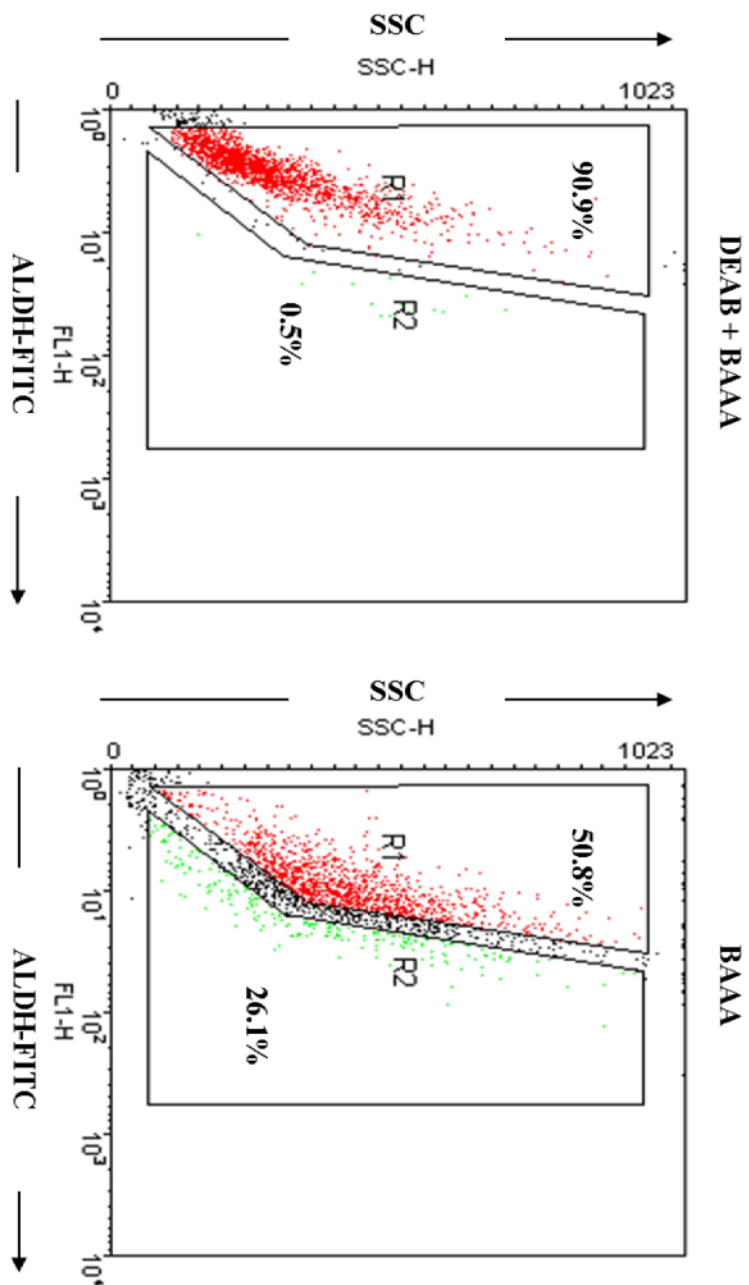
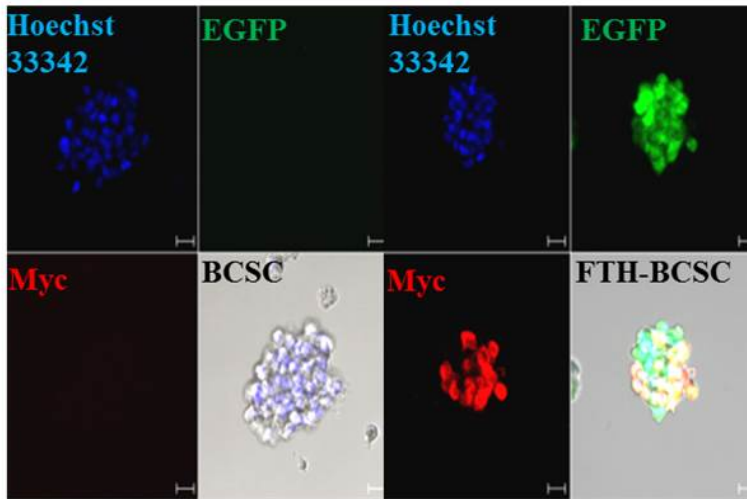


Figure 1–2. Aldehyde dehydrogenase activity of BCSCs. ALDH activity in BCSCs was analyzed and showed shifted populations in BCSCs.

A



B

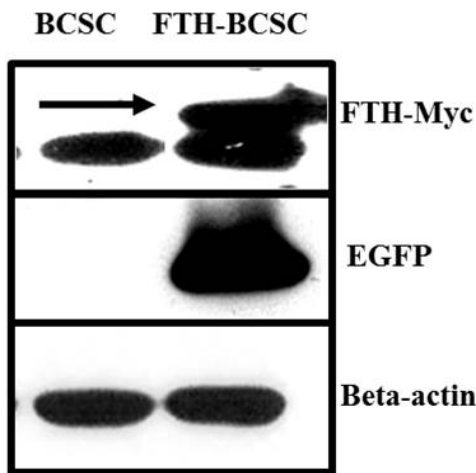


Figure 1–4. Establishment of FTH–BCSCs.

(A) Immunocytochemistry of BCSCs and FTH–BCSCs (bar, 50 μ m). (B) Western blot analysis for myc–FTH and EGFP in BCSCs and FTH–BCSCs.

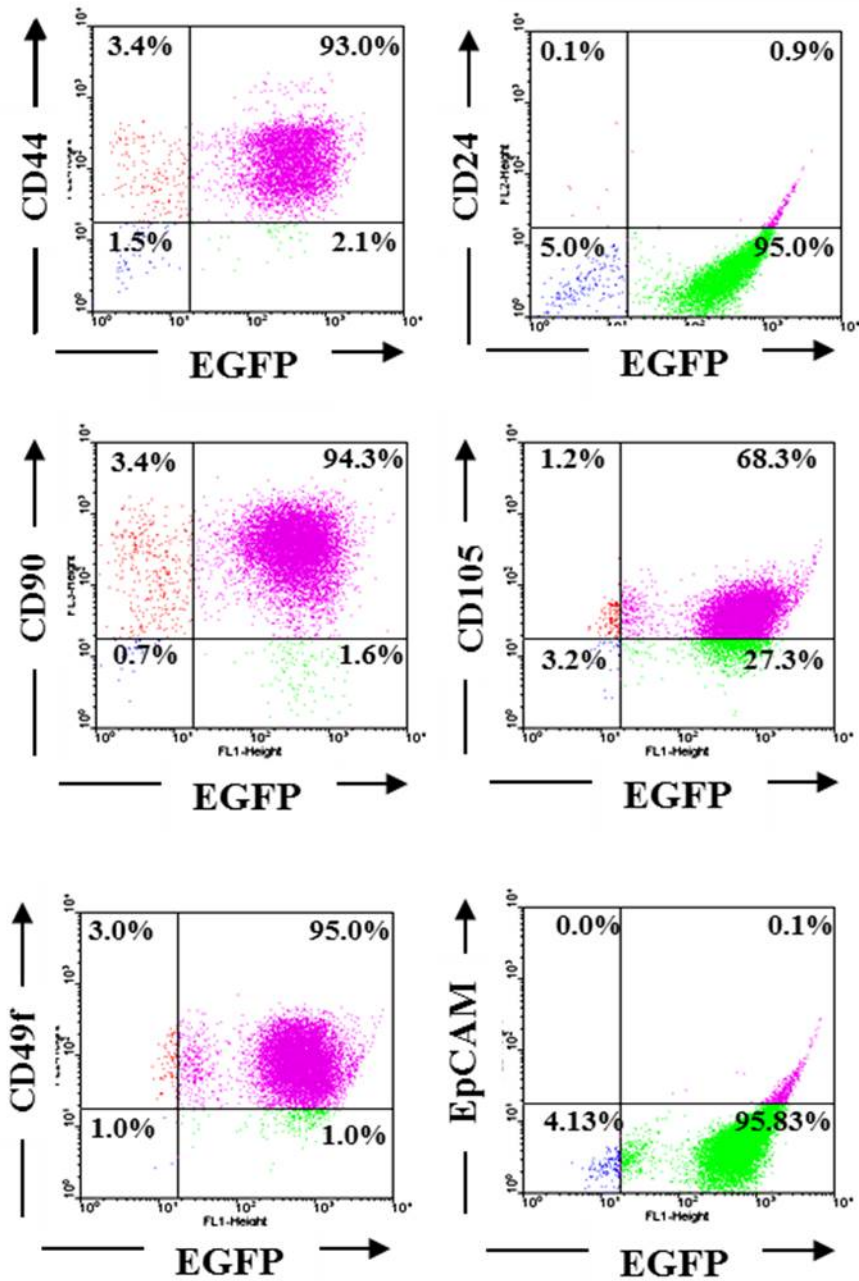
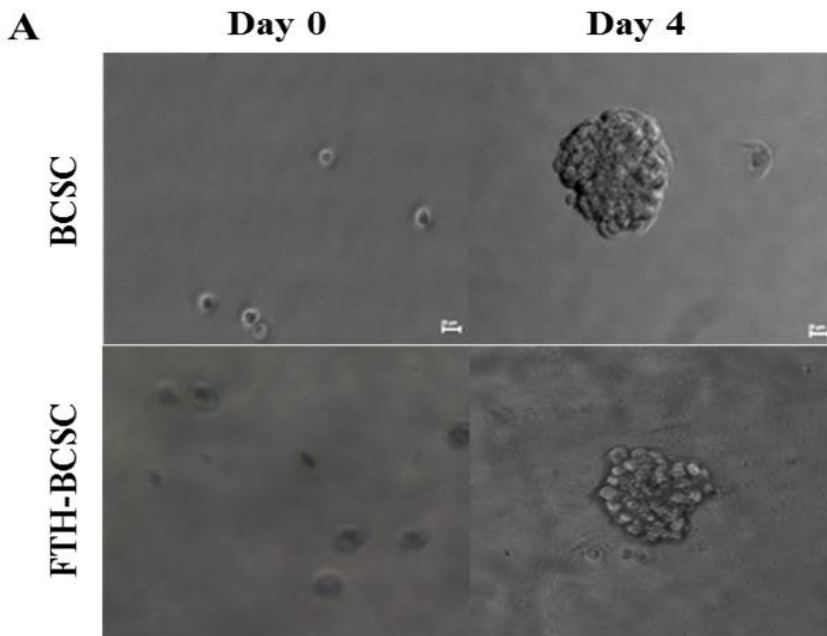


Figure 1–5. Biological characteristics of FTH-BCSCs.

CD marker expression levels of FTH-BCSCs were similar to those of BCSCs (CD44⁺, CD24⁻, CD49f^{high}, CD90^{high}, CD105^{high} and EpCAM^{low}).



B

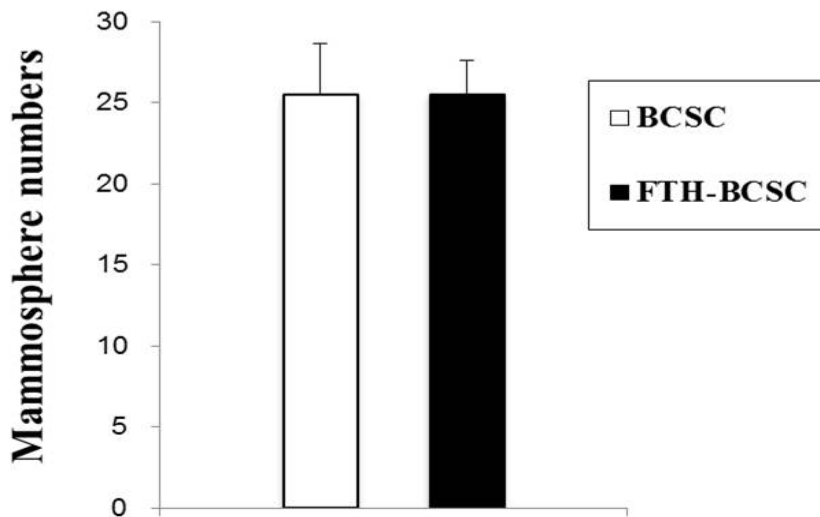


Figure 1–6. Mammosphere forming ability assay.

The abilities to form mammospheres did not differ between BCSCs and FTH–BCSCs.

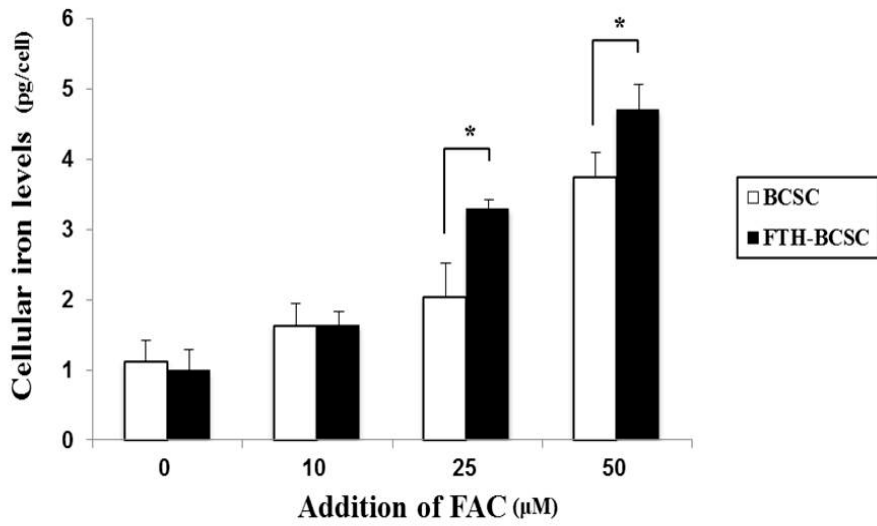


Figure 1–7. Measurement of cellular iron levels.

Cellular iron levels were measured in BCSCs and FTH–BCSCs treated with increasing concentration of ferric ammonium citrate (FAC, 0–50 μM).

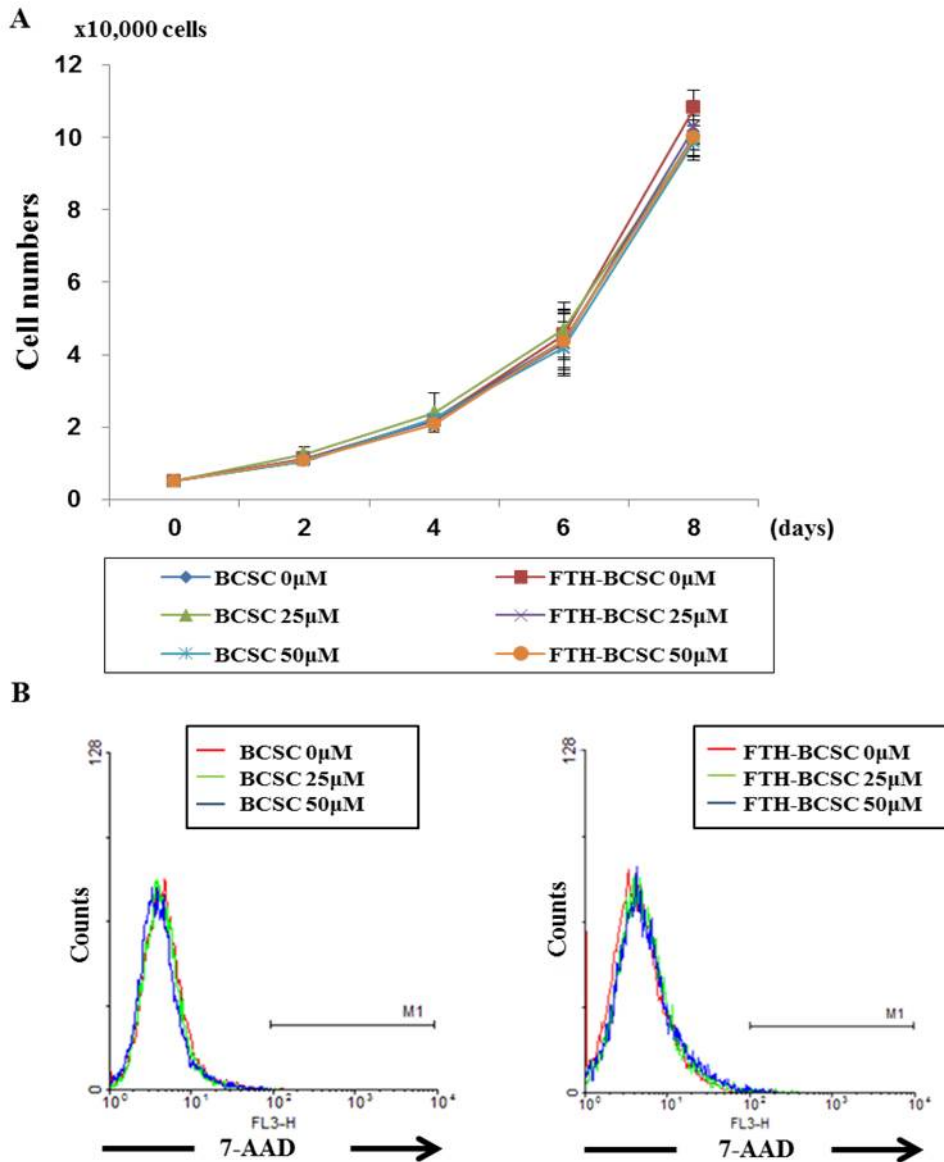
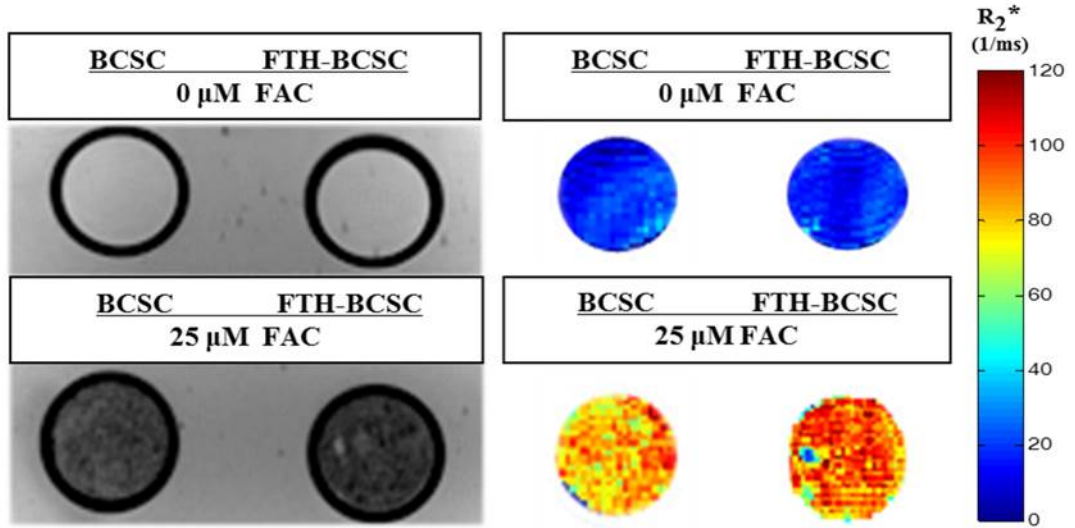


Figure 1–8. Cell growth analysis and the 7–AAD assay with iron supplementation.

(A) There was no significant difference in the growth rates of the BCSCs and FTH–BCSCs in the presence of an iron supplement (FAC). (B) The 7–AAD assay revealed that the viabilities of the BCSCs and FTH–BCSCs in the presence of the iron supplement were not significantly different.

A



B

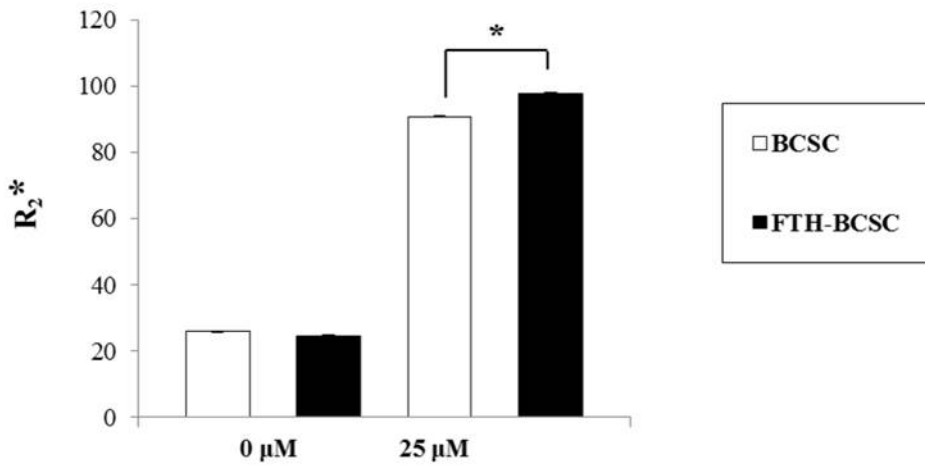


Figure 1–9. MRI phantom images and analysis.

(A) In vitro MRI images (left) and color-coded maps (right) of agarose phantoms of BCSCs and FTH-BCSCs treated with or without 25 μM FAC. (B) R_2^* values measured from MRI images of BCSC and FTH-BCSC phantoms. * $P < 0.05$.

DISCUSSION

This study demonstrated that the lentivirus mediated FTH and EGFP overexpression can be applied for tracking and imaging BCSCs without any disruption in breast tumorigenic cell properties by using MRI scanner and fluorescence images. Any changes at all in the characteristics of BCSCs were detected even after delivery of ferritin gene into BCSCs. Both BCSCs and FTH-BCSCs showed basal-like (CD44+/CD24-) (34-36) and mesenchymal-like phenotype (37, 38) that presumed as BCSCs with concerns of normal mammary stem cell development and epithelial-mesenchymal transition event by previous studies.

Accumulation of iron in the cancer cells may have adverse effects on the host since iron is pivotal nutrient for proliferation and growth in normal cells as well as cancer cells. Some studies reported high iron concentration promoted the cancer cell proliferation by overexpressing transferrin receptor that could elevate the level of reactive soluble iron in cells (39). However, the study reported by Cohen et al. (22) and the results from this study demonstrated iron accumulation by ferritin overexpression did not alter breast cancer cell proliferation and viability in vitro (25). These results suggest that ferritin overexpression can detoxify the

reactive free iron not to affect the proliferation and growth of cancer cell, even the increase in net intracellular iron amount by inducing iron uptake.

In conclusion, this study showed the possibility for providing valuable information of BCSCs behavior and their physiology in living subjects by combination of MRI and fluorescence imaging modalities. Furthermore, the applications of dual image methods in animal model will be useful to understand the breast tumors originated from cancer stem cells and to develop novel therapeutics for chemotherapy or radiotherapy-resistant tumor and recurrent tumor.

CHAPTER 2

Noninvasive identification of viable cell populations in docetaxel–treated breast tumors

INTRODUCTION

Although many MRI studies of a single or xenografted cancer cells were performed by using nanoparticles or commercially available contrast agents (40–42), there are some limits to apply contrast agents guided MR imaging of cancer cells. Contrast agents can successfully image cells in the single–cell resolutions, but it is difficult to visualize the newly generated tumor cells. As death of cancer cells can cause the contrast agent lost, only size measurement of the tumors can be used to evaluate the effects of anti–cancer therapies and quantification of contrast agents in tumors does not reflect the precise anti–cancer drug effects. However, MR imaging of BCSCs using lentivirus mediated MR reporter gene can visualize the newly generated tumor cells and longitudinal monitoring can identify the viable cell population in the tumors when anti–cancer drugs are treated. In addition, using lentivirus mediated reporter gene expression can overcome the challenge of delivering contrast agents to deep tissues (25). Up to date, in vivo imaging of BCSCs using MR reporter gene has not been reported.

In this study, FTH–BCSCs were monitored after the treatment of docetaxel with the advantage of longitudinal monitoring of MR

reporter. Viable cell populations were distinguished from non-viable cell populations in docetaxel treated tumors which was intriguing because previous techniques with MRI are not able to distinguish the viable and non-viable cell populations easily if tumors don't have any necrotic area. In addition, complementary use of fluorescence and MRI will allow fast and sensitive imaging and visualize precise anatomical structures (43-45).

MATERIALS AND METHODS

1. Ethics statement

In animal study, 6-week-old NOD/SCID female mice were used. The animal study was reviewed and approved by the Institutional Animal Care and Use Committee (IACUC; No.11-0105) of the Seoul National University Hospital, and the procedures for all animal experiments were performed according to IACUC guidelines.

2. Tumor formation and tumor volume measurements

To compare the tumor formation abilities of BCSCs and FTH-BCSCs, 2×10^2 – 1×10^6 viable BCSCs and FTH-BCSCs were implanted into the mammary fat pads of NOD/SCID mice (BCSC tumors [n=21]; FTH-BCSC tumors [n=21]). Tumor formation was monitored up to eight weeks after implantation, depending on the number of injected cells.

3. Fluorescence imaging

At three weeks post-injection, the fluorescence imaging of BCSC and FTH-BCSC tumors from a living mouse was assessed using a Maestro imaging system (CRi Inc.) with excitation and emission set at 445–490 nm and 515 nm, respectively. The filter was adjusted

while the camera captured images, and the signals from the tumors were merged with a GFP-filtered image.

Ex vivo fluorescence imaging of BCSC and FTH-BCSC tumors excised from mice was performed by GFP fluorescence analysis (excitation: 470 nm, emission: 535 nm) using a Kodak Image Station 4000MM (Carestream Molecular Imaging).

4. Docetaxel treatment and cytotoxicity assays

To investigate the in vitro cytotoxicity of docetaxel on BCSCs and FTH-BCSCs, JC-1 staining and 3-(2,5-diphenyltetrazolium bromide) (MTT) assays were performed following treatment with docetaxel (1-10 nM, Sigma-Aldrich Chemical Co.) for 24 hours. To evaluate the changes in the mitochondrial membrane potential of both cell populations treated with docetaxel, the mitochondrial vital dye JC-1 (10 μ g/ml, Invitrogen) was used. JC-1 aggregates with intense red fluorescence are known to accumulate in the intact mitochondria of healthy cells. When the mitochondrial membrane potential collapses in non-viable cells, JC-1 monomers fluoresce green. The percentage of cells with intact mitochondrial membranes was calculated by dividing the number of red fluorescence-positive cells by the total cell number.

5. In vivo docetaxel treatment and tumor volume measurement

The mice with BCSC (n=18) and FTH-BCSC (n=18) tumors were divided into docetaxel-treated (n=19) and untreated control groups (n=17). Docetaxel was treated when the tumor volumes had 70 mm^3 , usually 16 to 18 days after tumor cell implantation. In the docetaxel-treated groups, docetaxel (15 mg/kg) was injected into the tail vein of mice three times at intervals of 72 hours to evaluate the therapeutic effect of docetaxel on BCSC and FTH-BCSC tumors. The BCSC and FTH-BCSC tumors in the docetaxel-treated group are represented as BCSC Doc tumors (n=10) and FTH-BCSC Doc tumors (n=9), respectively. In the control group (BCSC tumors [n=8]; FTH-BCSC tumors [n=9]), saline was intravenously injected three times at the same intervals as those used in the docetaxel-treated groups.

To determine the volumes of the BCSC and FTH-BCSC xenograft tumors, a modified ellipsoidal formula for volume (volume = $1/2[\text{length} \times \text{width}^2]$) was used, in which length was the measurement of the greatest longitudinal diameter and width was the greatest transverse diameter.

6. MRI examination

MRI studies were performed on a 9.4-T BrukerBiospec scanner (BrukerBiospin). A transmit-only volume coil and a four-channel surface coil (BrukerBiospin) were used for excitation and signal reception, respectively.

For in vivo MRI of mice bearing xenograft tumors, 1×10^6 BCSCs or FTH-BCSCs were injected into the mammary fat pads of NOD/SCID mice. For whole-animal MRI, mice were anesthetized with isofluorane (1% in 100% oxygen). To stabilize the body temperature of the mice during MRI experiments, an animal warming system (BrukerBiospin) was used. Pre-treatment images were obtained three weeks after injection, and longitudinal follow-up images were obtained at 5 and 14 days after docetaxel treatment. In vivo data were acquired for fat saturation. The parameters were as follows: matrix size = 256 x 256, TR = 5000 ms, slice thickness = 1 mm (no gap), flip angle = 90° , FOV = 37 x 37 mm², TE = 3.1–34.4 ms with a step size of 4.4 ms (eight-point T_2^* mapping), 17 slices and 1 signal average.

7. MRI data analysis

All data post-processing was performed with Matlab (Mathworks Inc.). For MR data, regions of interest (ROIs) were defined in each individual, imaging slices were acquired at the shortest TE and T_2^* maps of the ROIs were later estimated by pixel-by-pixel analyses across the multi-point MRI images, assuming single exponential decay. After performing the R_2^* analyses, R_2^* color maps were merged with the anatomical images acquired at the shortest TE. For in vivo data, volumetric tumor images were reconstructed from the entire set of 2D slices for each animal.

To investigate the differences in the R_2^* distribution among the animal groups, we obtained R_2^* histograms for each animal by including all pixels in the ROIs across all slices. Comparisons of the mean R_2^* values among the animal groups were performed based on the R_2^* distributions. Additionally, to represent the differences in the R_2^* distribution better, we defined the mean plus 3 standard deviation (mean + 3 SDs) as a threshold. The distribution of skewedness was analyzed using the threshold values of each group and subsequent pixel percentages. In addition, the mean R_2^* values of the pixels over the threshold values of each group of tumors were calculated for the comparison of the R_2^* value distribution of each group of tumors.

8. Defining mean + 3 SDs threshold

The R_2^* distribution of the entire histogram was obtained by calculating the values from all tumor slices of each group with intervals of three slices. Then, the pixel percentage of the R_2^* values greater than the mean + SD (mean plus standard deviation), mean + 2SDs and mean + 3SDs values of each group was obtained by dividing the number of pixels with the values corresponding to mean + SD, mean + 2SDs and mean + 3SDs in the tumor histograms of each group by the number of pixels in all of the histograms and subsequently multiplying that number by 100. The mean + SD, mean + 2SDs and mean + 3SDs pixel percentages of each group were calculated (data not shown), and the mean + 3SDs value that best represented the skewedness of the FTH-BCSC Doc tumors was defined as the threshold.

9. Histochemical analysis of tumors

After MRI examination, the excised tissues were fixed with 10% buffered formalin and embedded in paraffin blocks. Tissues were sectioned into 4- μm -thick sections. Hematoxylin and eosin staining (H&E) was performed to distinguish the viable and nonviable cell

populations within the tumors. Immunofluorescence staining for the surface markers CD44 and CD24 and the proliferative marker phospho-histone 3 (PH3) were performed. After incubation of tissue sections with a blocking solution for one hour at room temperature, primary antibodies against CD44 (Thermo Scientific), CD24 (Novus Biologicals), or PH3 (Novus Biologicals) were incubated overnight at 4° C. Next, fluorescence-conjugated antibodies, namely, anti-mouse IgG Alexa 488, 647 or anti-rabbit IgG Alexa 594 (Invitrogen), were incubated for 45 minutes at room temperature. Hoechst 33342 (Invitrogen) was used to visualize the cell nuclei. Immunofluorescence images of the tissue sections were obtained under a confocal laser microscope (Carl Zeiss) and a fluorescence microscope (Leica).

10. Statistical analysis

All data are presented as the mean \pm SD for at least three independent experiments. The mean values of the data were statistically evaluated using ANOVA followed by an unpaired t-test. A Fisher' s exact test was used to analyze the differences in R_2^* value distributions. For all tests, P-values less than 0.05 or 0.01 were considered to be statistically significant.

RESULTS

Tumor forming abilities of FTH-BCSCs were not different from BCSCs

A tumor forming ability assay with serially diluted numbers of BCSCs and FTH-BCSCs were performed to investigate whether ferritin overexpression affects tumorigenesis *in vivo*. Various numbers of BCSCs or FTH-BCSCs were xenografted into the mammary fat pads of mice, and the incidence of the BCSC and FTH-BCSC tumors following engraftment with 2×10^2 cells was approximately 25% with transplantation of more than 1×10^3 BCSCs or FTH-BCSCs, resulting in 100% tumor formation (Table 2-1). The sizes of the BCSC and FTH-BCSC tumors were similar. Ex vivo fluorescence imaging showed the stable expression of EGFP in the FTH-BCSC tumors (Figure 2-1). These results demonstrated that the FTH-BCSCs retained the characteristics of BCSCs, despite the overexpression of FTH and EGFP.

FTH-BCSCs tumor showed significant increase in R_2^* values in MRI compared to BCSC tumor

Next, the effect of ferritin overexpression in a xenograft tumor model was investigated *in vivo* MRI as previous *in vitro* MRI showed

the feasibility of FTH as a MR reporter. Lower signal intensities were observed in the MRI images of FTH-BCSC tumors compared with BCSC tumors due to ferritin overexpression (Figure 2-2A, left). A color-coded map of BCSC and FTH-BCSC tumors revealed variable R_2^* values (Figure 2-2A, right). Although both the BCSC and FTH-BCSC tumors exhibited differences in the R_2^* values within the tumors, the FTH-BCSC tumors exhibited higher mean R_2^* values compared with the BCSC tumors, and the FTH-BCSC tumors exhibited shifted R_2^* distributions toward higher R_2^* values (Figure 2-2B; mean R_2^* values of BCSC tumors vs. FTH-BCSC tumors; $87.2 \pm 2.7s^{-1}$ vs. $105.4 \pm 3.8s^{-1}$; $P < 0.01$).

MRI reveals distinct populations of pixels with high R_2^* values within docetaxel-treated FTH-BCSC tumors

To further use of FTH as a MR reporter for BCSCs monitoring the efficacy of an anti-cancer drug in xenografted tumors was evaluated. Before the experiments with FTH in anti-cancer drug monitoring, the growth of docetaxel-treated BCSC and FTH-BCSC tumors was observed and confirmed that the docetaxel attenuated BCSCs and FTH-BCSCs (BCSC Doc, FTH-BCSC Doc) growth

compared to BCSC and FTH-BCSC tumors. Overexpression of FTH did not affect tumor growth (Figure 2-3).

Subsequent slice-by-slice MRI analysis of tumors from each group was performed and observed different distributions of tumor R_2^* values in volumetric images with longitudinal follow-up scans (Figure 2-4 and 2-5). Before docetaxel treatment, the R_2^* value distribution between BCSC and BCSC Doc tumors and that between FTH-BCSC and FTH-BCSC Doc tumors were similar (Figure 2-6A and Table 2-2). At day 5 of docetaxel treatment, the mean R_2^* values of the BCSC Doc and FTH-BCSC Doc tumors were significantly decreased compared with the BCSC and FTH-BCSC tumors ($P < 0.05$; Figure 2-6B and Table 2). At day 14 of docetaxel treatment, the BCSC Doc and FTH-BCSC Doc tumors exhibited lower mean R_2^* values compared with the BCSC and FTH-BCSC tumors ($P < 0.01$; Figure 2-6C and Table 2-2). Notably, histogram analysis revealed that only the FTH-BCSC Doc tumors at day 14 of docetaxel treatment had distinct populations of pixels with high R_2^* values and a distribution of R_2^* values that was skewed compared with the other groups (Figure 2-6C). In the FTH-BCSC Doc tumors, pixels that represented a distinct population and were measured over the threshold value (mean + 3SDs; Table 2-3)

occupied approximately 50% of the total pixels, while the percentages of all the other groups were less than 30% ($P < 0.05$, Figure 2-7).

Histological analysis reveals that the cell populations with high R_2^* values are localized in viable areas of the FTH-BCSC tumors

Histological analysis was performed to investigate whether ferritin-based MRI images reflects the tissue state after docetaxel treatment. MRI showed that the R_2^* value pixels were similarly distributed between the periphery and center of both BCSC and FTH-BCSC tumors and H&E staining revealed that most of the cells in the periphery and center of the BCSC and FTH-BCSC tumors were viable (Figure 2-8A and C). In contrast, MRI showed that the R_2^* value pixels were differently distributed between the periphery and center of BCSC Doc and FTH-BCSC Doc tumors and H&E staining revealed that the center of BCSC Doc tumors with low R_2^* values had both viable and nonviable cell populations (Figure 2-8B, right), whereas the center of the FTH-BCSC Doc tumors with mixed high and low R_2^* values matched those of the viable and nonviable cells within the tumors, respectively (Figure 2-8D, right). In addition, the periphery of BCSC Doc and FTH-BCSC Doc tumors

with high R_2^* values had viable cells whereas viable cells were also found in the periphery of the BCSC Doc tumors with low R_2^* values (Figure 2-7B, left). The presence of viable cells in the FTH-BCSC and FTH-BCSC Doc tumors was confirmed with EGFP fluorescence (Figure 2-9). Additionally, we investigated the co-expression of myc-FTH and EGFP in the FTH-BCSC and FTH-BCSC Doc tumors and confirmed that the EGFP-positive cells had the myc-FTH expression (Figure 2-9).

To clarify whether ferritin overexpression alters the therapeutic response to docetaxel, cell viability was evaluated by mitochondrial membrane potential analysis and MTT assay after treatment with docetaxel. Docetaxel induced a depolarization of the mitochondrial membrane potentials and reduced the intact mitochondria in both BCSCs and FTH-BCSCs (Figure 2-10A). A decrease in cell viability in the FTH-BCSCs and BCSCs were observed in a docetaxel dose-dependent manner using MTT assay and 7-AAD assay (Figure 2-10B-D). There was no significant difference in the change of mitochondrial membrane potential and cell viability between FTH-BCSCs and BCSCs after treatment with docetaxel. Thus, we conclude that the ferritin overexpression did not affect the BCSCs' response to docetaxel treatment.

The viable cell populations within the tumors exhibit the BCSC phenotype and high levels of proliferative markers

To investigate the effects of docetaxel treatment on FTH-BCSC tumors, double staining for CD44 and CD24 was performed on FTH-BCSC and FTH-BCSC Doc tumors. Because the cells located in the periphery and center of the tumor responded differently to docetaxel, CD44 and CD24 expression was analyzed in both regions (Figure 2-11A). The periphery of the FTH-BCSC Doc tumors contained significantly higher proportions of CD44+/CD24- BCSCs compared to the periphery and center of the FTH-BCSC tumors (FTH-BCSC periphery and center: $58.46 \pm 2.07\%$ and $44.35 \pm 4.82\%$; FTH-BCSC Doc periphery and center: $71.38 \pm 3.75\%$ and $56.13 \pm 5.92\%$, $P < 0.05$) (Figure 2-11B). CD44+/CD24+ and CD44-/CD24- cells were detected in the periphery and center of FTH-BCSC and FTH-BCSC Doc tumors. However, the proportion of these cells was not significantly different between FTH-BCSC and FTH-BCSC DOC tumors.

We investigated the cell proliferation marker PH3 to determine whether docetaxel alters tumor cell proliferation. The percentage of cells expressing PH3 in the EGFP-positive cell population was

analyzed in the periphery and center of FTH-BCSC and FTH-BCSC Doc tumors. Significantly higher percentage of PH3-positive cells were observed in the periphery and center of the FTH-BCSC Doc tumors (FTH-BCSC periphery and center: $0.97 \pm 0.04\%$ and $0.83 \pm 0.19\%$, FTH-BCSC Doc periphery and center: $11.48 \pm 0.90\%$ and $9.32 \pm 1.38\%$, $P < 0.01$) (Figure 2-12A and B).

Table 2–1. Evaluation of the incidence of tumors in NOD/SCID mice implanted with different numbers of BCSCs and FTH–BCSCs.

Cell type	Cell numbers	Tumor incidence
BCSC	1×10^6	3/3
	1×10^5	6/6
	1×10^4	4/4
	1×10^3	4/4
	2×10^2	1/4
FTH–BCSC	1×10^6	3/3
	1×10^5	6/6
	1×10^4	4/4
	1×10^3	4/4
	2×10^2	1/4

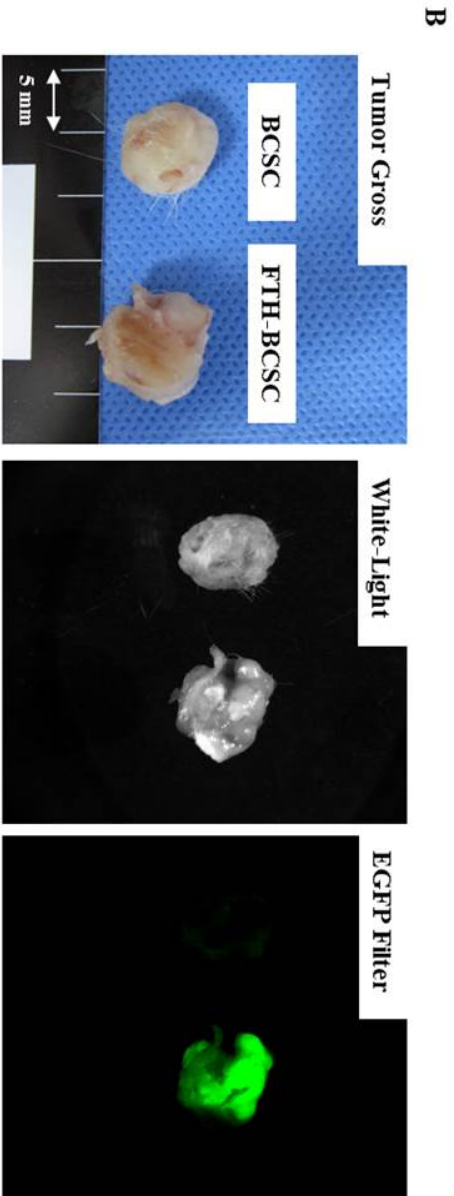
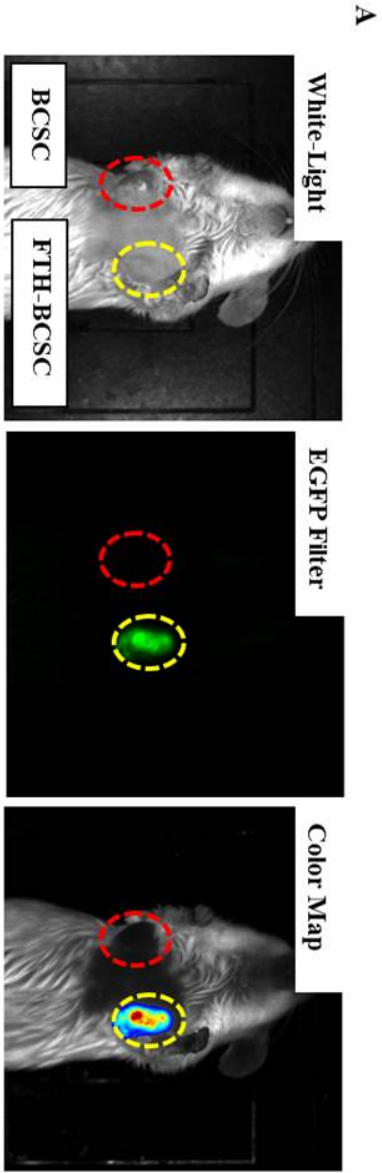


Figure 2–1. Comparison of tumor–forming abilities and fluorescence imaging of BCSCs and FTH–BCSC–derived tumors.

(A) Tumor–forming abilities were similar for BCSCs and FTH–BCSCs, and in vivo live imaging confirmed that only the FTH–BCSC tumors expressed EGFP fluorescence. The red dotted circle indicates the BCSC tumor and the yellow dotted circle indicates the FTH–BCSC tumor. (B) Ex vivo EGFP fluorescence of image excised tumors derived from BCSCs and FTH–BCSCs. The sizes of the BCSCs and FTH–BCSC tumors were similar.

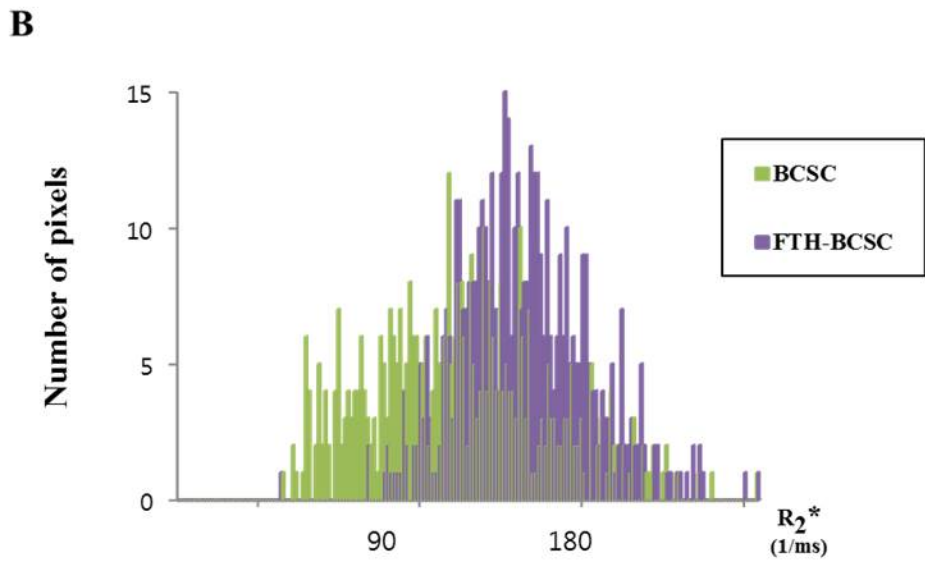
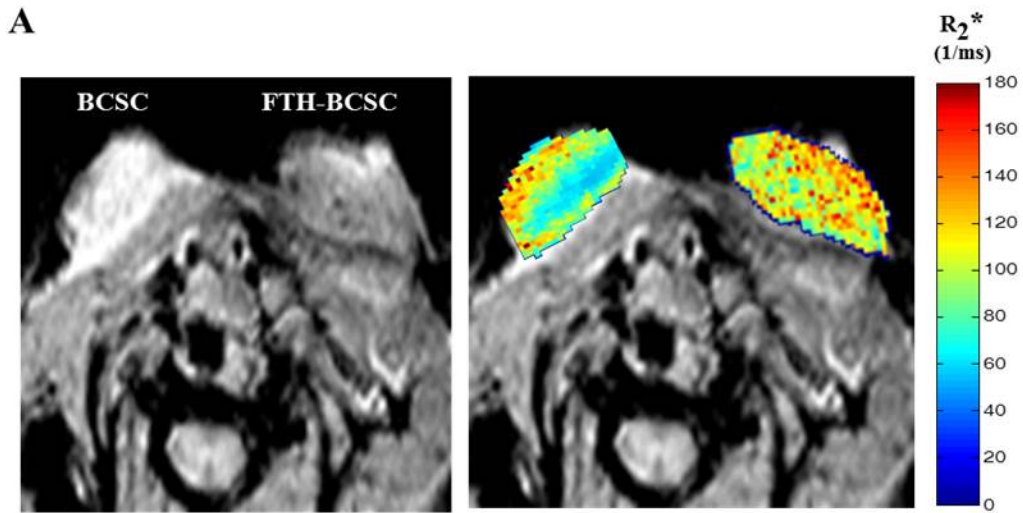


Figure 2–2. MRI images of xenograft tumors.

(A) In vivo MRI images (left) and color–coded maps (right) of BCSC and FTH–BCSC xenograft tumors in the mammary fat pads of NOD/SCID mice. (B) The distributions of the R_2^* values obtained for the BCSC and FTH–BCSC tumors at 3 weeks post–transplantation.

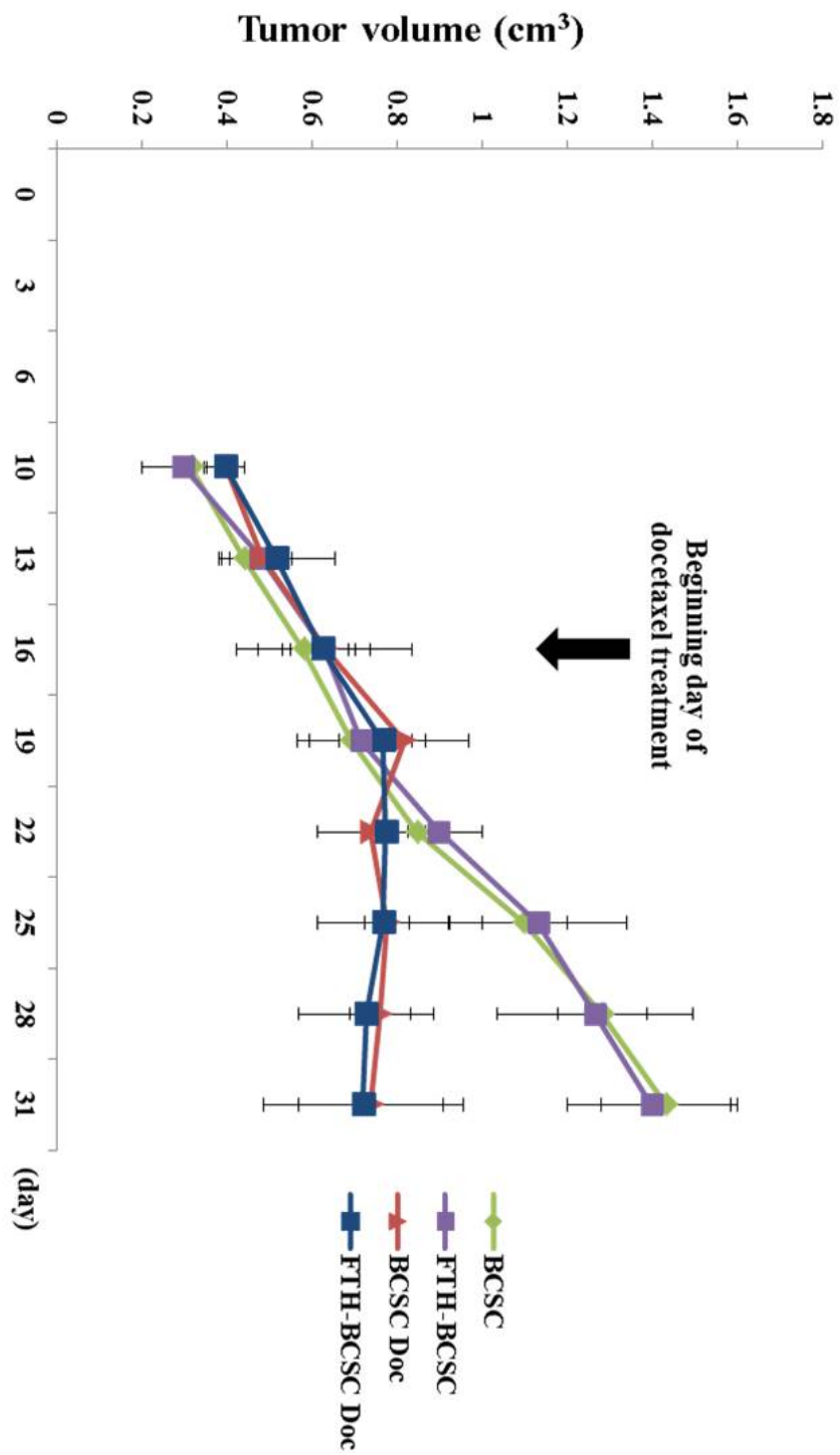


Figure 2–3. Growth rates of BCSC, FTH–BCSC, BCSC Doc and FTH–BCSC Doc tumors.

BCSCs and FTH–BCSCs (1×10^6) were engrafted into the mammary fat pads of NOD/SCID mice. Mice ($n = 5$ per group) were treated with i.v. injections of docetaxel (15 mg/kg) at three–day intervals beginning the day after the pre–treatment MRI. Tumor growth was attenuated in BCSC Doc and FTH–BCSC Doc tumors 5 days after docetaxel treatment, and FTH overexpression did not affect the tumor growth rate in either the docetaxel–untreated or treated groups (BCSC vs. FTH–BCSC tumors, BCSC Doc vs. FTH–BCSC Doc tumors). The bars in the graph represent SDs.

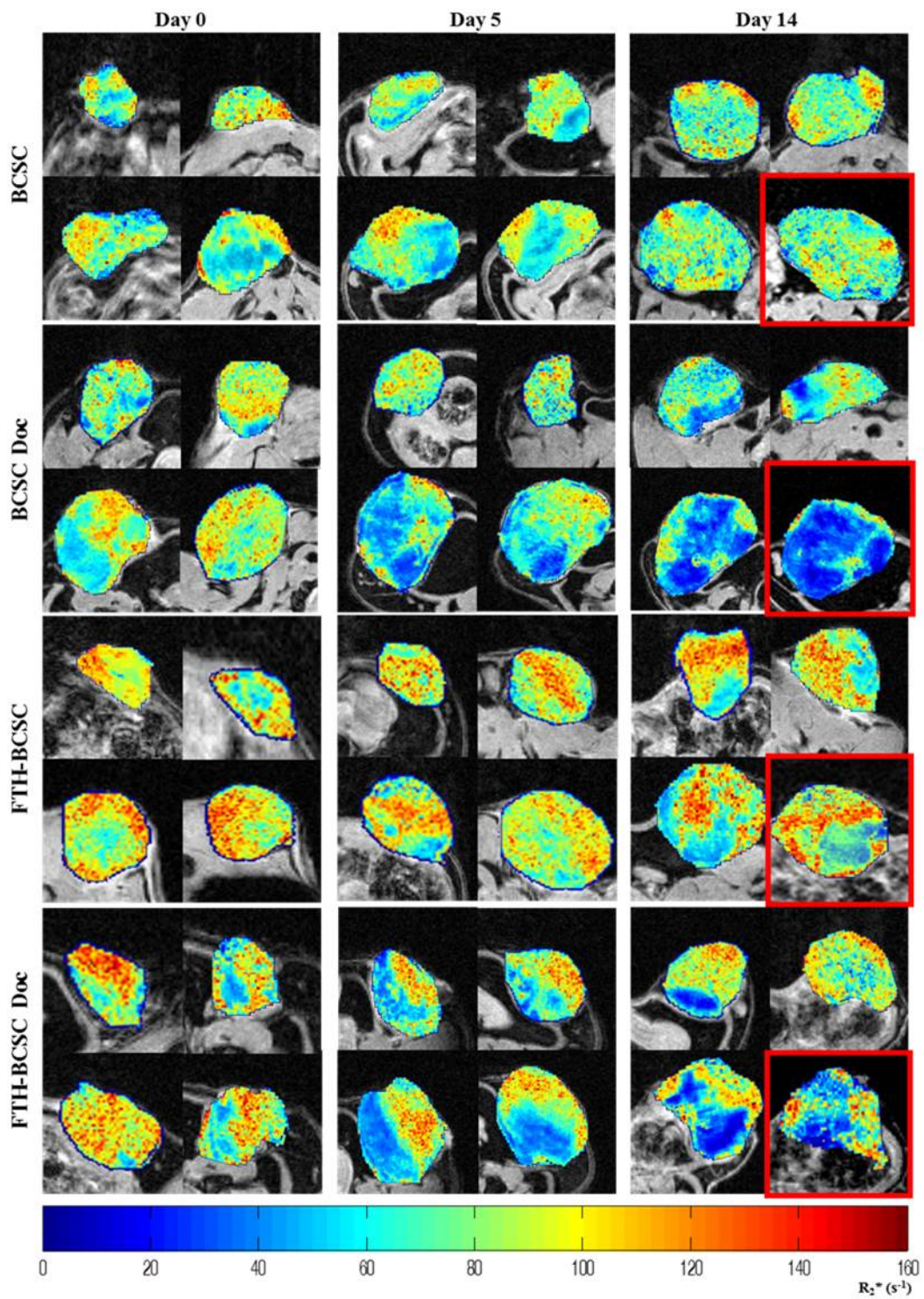


Figure 2-4. Slice-by-slice analysis of R_2^* values in the xenograft tumors.

Four representative slices from each group of tumors (BCSC, BCSC Doc, FTH-BCSC and FTH-BCSC Doc tumors) at day 0, day 5 and day 14 were processed with MATLAB. MRI Images in red box at day 14 were used in Figure 4. Color map range of R_2^* values: 0-160 (sec^{-1})

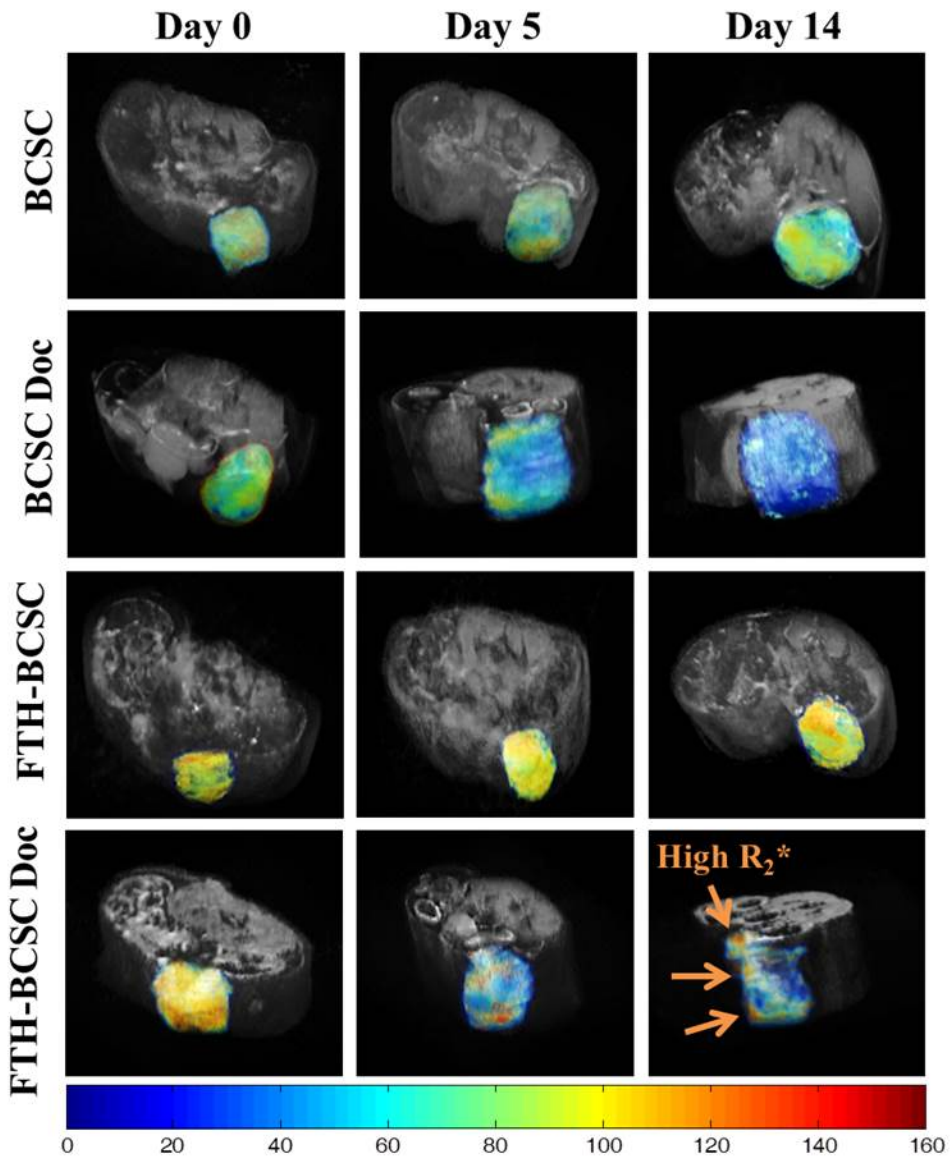


Figure 2–5. Volumetric MRI images of control (BCSC and FTH–BCSC) and docetaxel–treated (BCSC Doc and FTH–BCSC Doc) xenograft tumors.

Follow–up volumetric MRI images of BCSC, BCSC Doc, FTH–BCSC and FTH–BCSC Doc tumors.

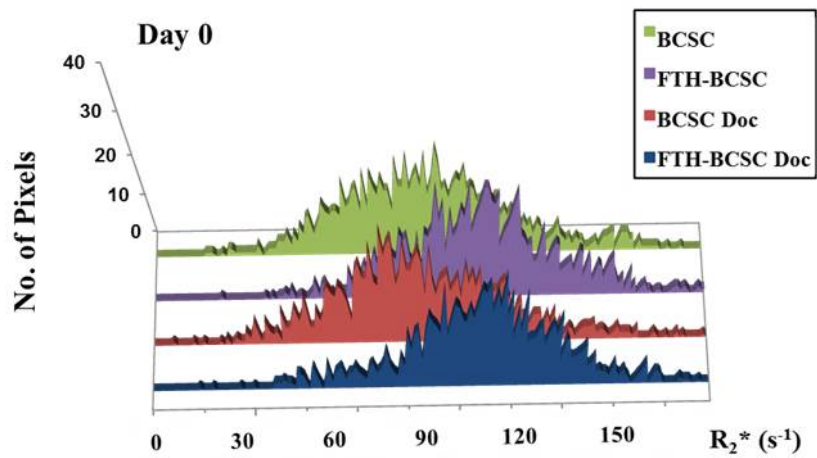
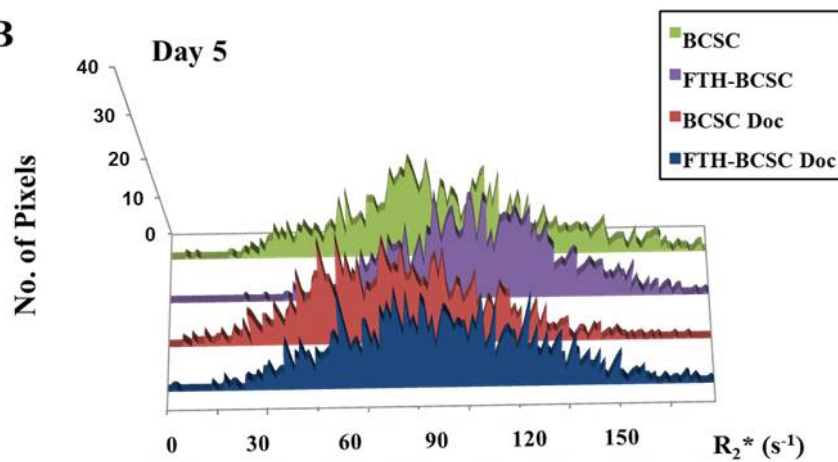
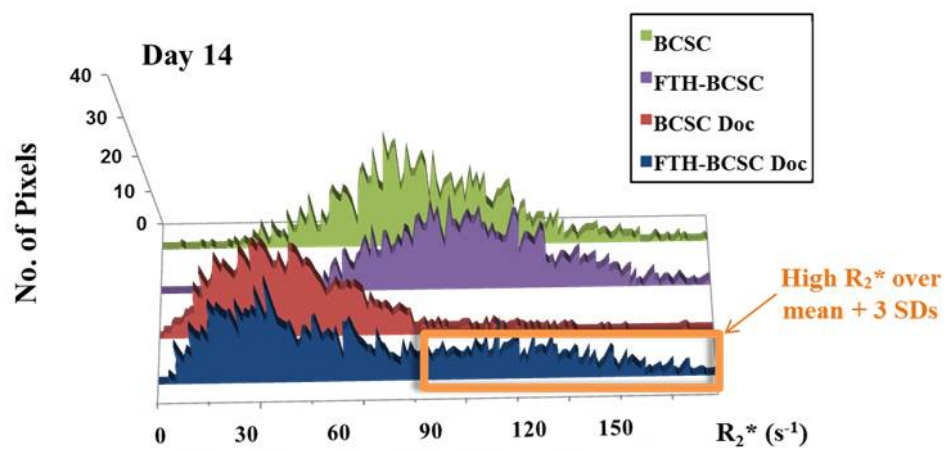
A**B****C**

Figure 2–6. Distribution of R_2^* values in control (BCSC and FTH–BCSC) and docetaxel–treated (BCSC Doc and FTH–BCSC Doc) xenograft tumors.

(A–C) Distribution of R_2^* values in BCSC, FTH–BCSC, BCSC Doc and FTH–BCSC Doc tumors at day 0, 5 and 14. The orange box indicates the pixels over the threshold (mean + 3 SDs) in the FTH–BCSC Doc tumors.

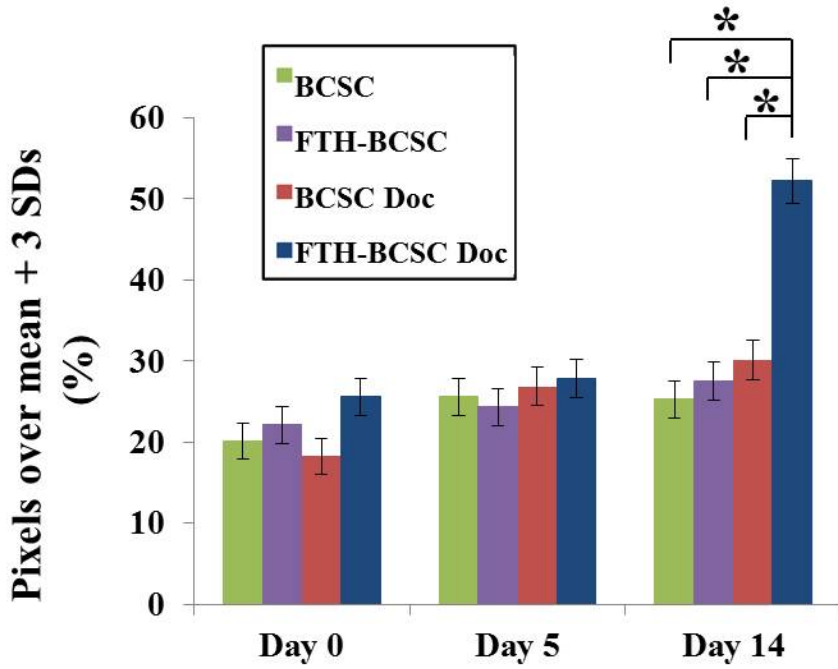


Figure 2-7. Analysis of pixels over threshold (mean + 3 SDs). Analysis of the percentage of pixels over the threshold (mean + 3SDs) in each tumor group. *P<0.05.

Table 2–2. Mean R_2^* values of control (BCSC and FTH–BCSC) and docetaxel–treated (BCSC Doc and FTH–BCSC Doc) xenograft tumors.

	Mean R_2^* value \pm SD (sec^{-1})		<i>P</i> value
	BCSC	BCSC Doc	
Day 0	83.30 \pm 6.30	79.47 \pm 8.30	0.12
Day 5	81.78 \pm 6.58	65.11 \pm 5.49	0.03 *
Day 14	79.47 \pm 8.30	43.32 \pm 7.89	0.001 **
	FTH–BCSC	FTH–BCSC Doc	
Day 0	96.94 \pm 8.45	95.96 \pm 8.69	0.18
Day 5	94.99 \pm 8.20	76.92 \pm 8.34	0.02 *
Day 14	91.24 \pm 7.71	55.26 \pm 9.16	0.001 **

NOTE: Values in bold are statistically significant (*, $P < 0.05$ and **, $P < 0.01$).

Table 2–3. R_2^* threshold values of docetaxel–untreated (BCSC and FTH–BCSC) and docetaxel–treated (BCSC Doc and FTH–BCSC Doc) xenograft tumors at day 0, day 5 and day 14.

Tumors	Day 0	Day 5	Day 14
BCSC	102.92	103.99	104.38
FTH–BCSC	122.3	119.59	114.4
BCSC Doc	104.38	77.97	67.01
FTH–BCSC Doc	122.54	95.15	82.75

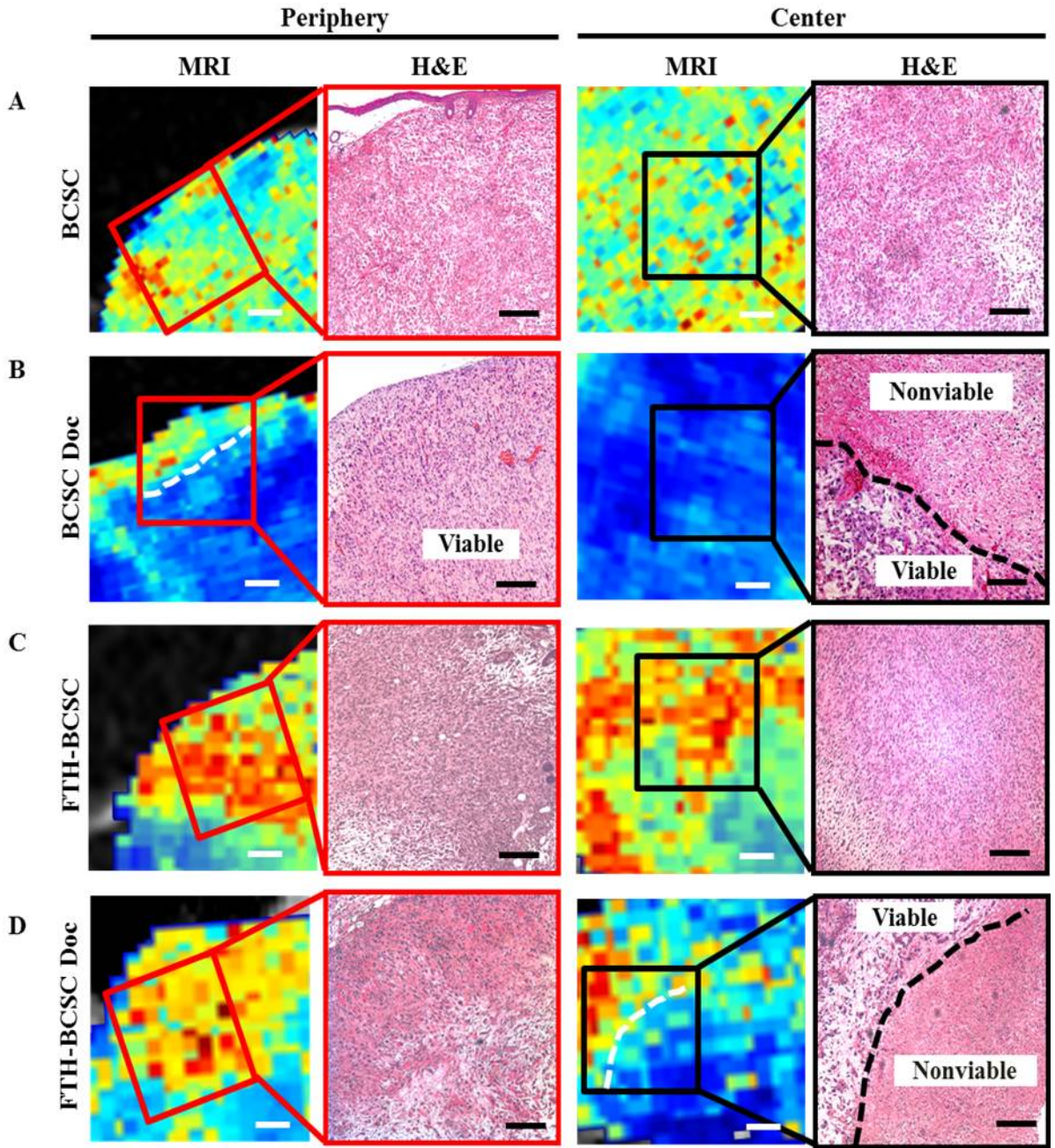


Figure 2–8. Histological analysis of the peripheral and central portions of control and docetaxel–treated xenograft tumors. (A–D) MRI images and H&E staining of BCSC, BCSC Doc, FTH–BCSC and FTH–BCSC Doc tumors obtained 4 weeks after the implantation. The red and the black boxes on the MRI images indicate the corresponding areas to H&E staining images of the periphery and the center of each tumor. The white dotted lines on the MRI images indicate the boundary where the R_2^* values were differed in the BCSC Doc and FTH–BCSC DOC tumors. The black dotted lines on H&E staining indicate the demarcation between viable and nonviable cells area in the central portions of the BCSC Doc and FTH–BCSC Doc tumors (x100; bar in H&E, 100 μ m, bar in MRI, 500 μ m).

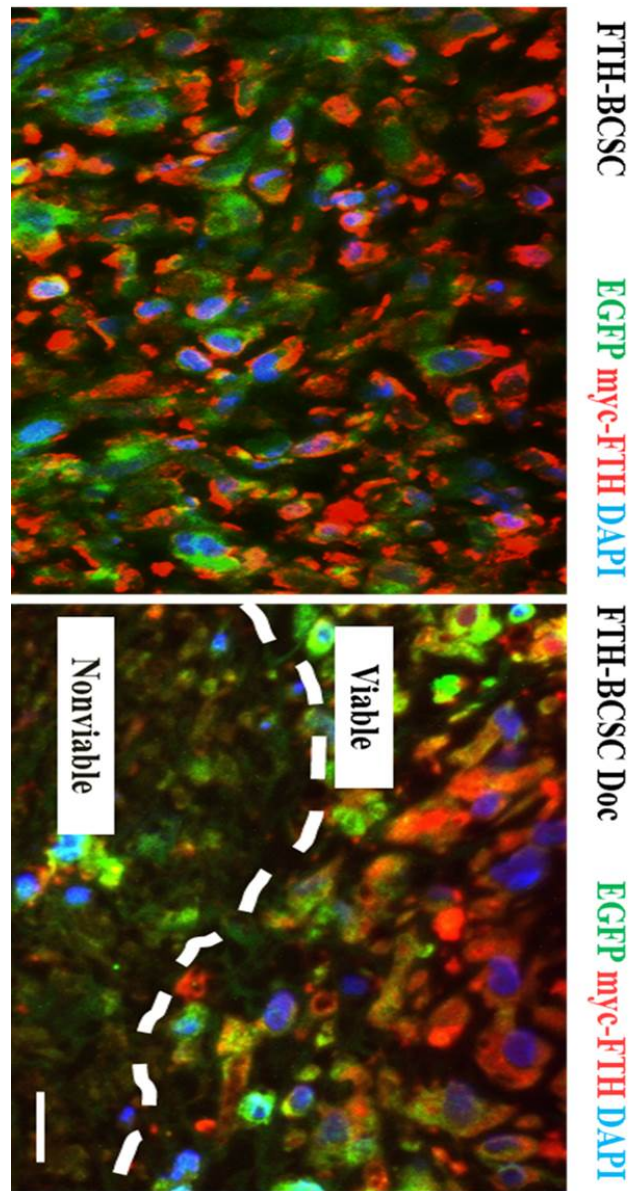


Figure 2–9. Immunostaining of EGFP and myc–FTH in FTH–BCSC and FTH–BCSC Doc tumors.

The white dotted line indicates the demarcation between the areas of viable and nonviable cells in the central portion of FTH–BCSC Doc tumors (x400; bar, 50 μ m).

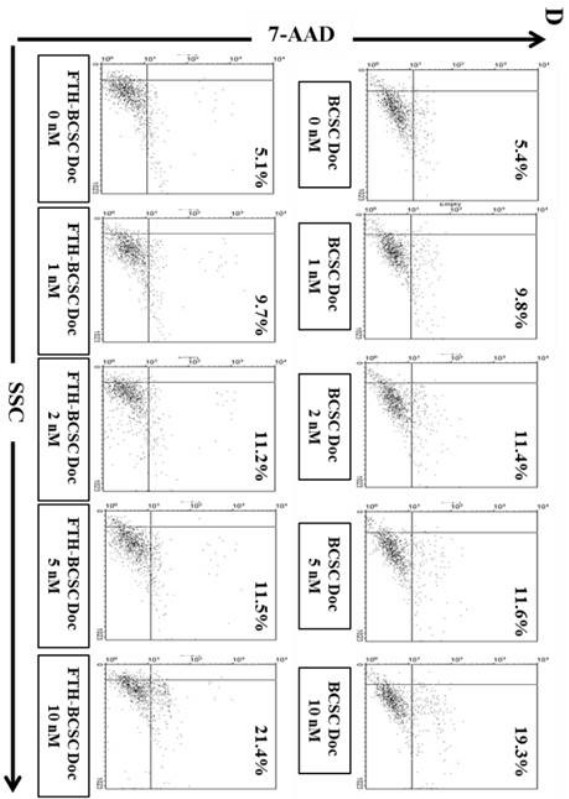
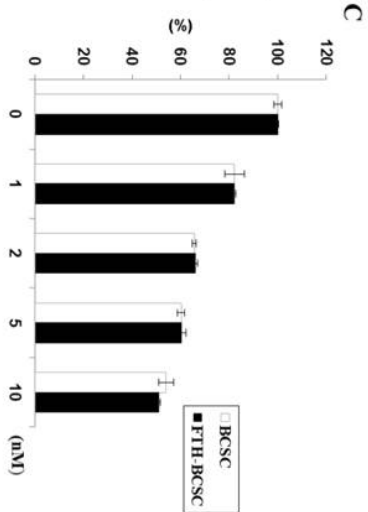
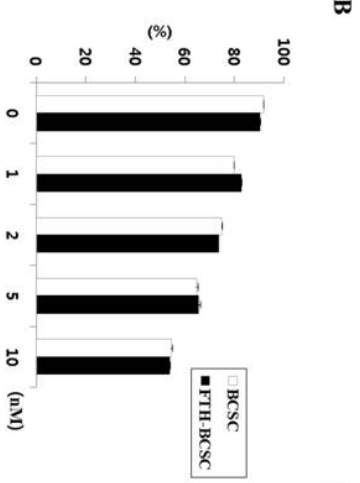
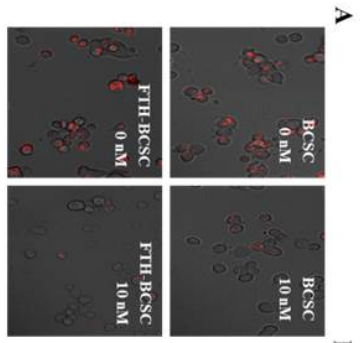
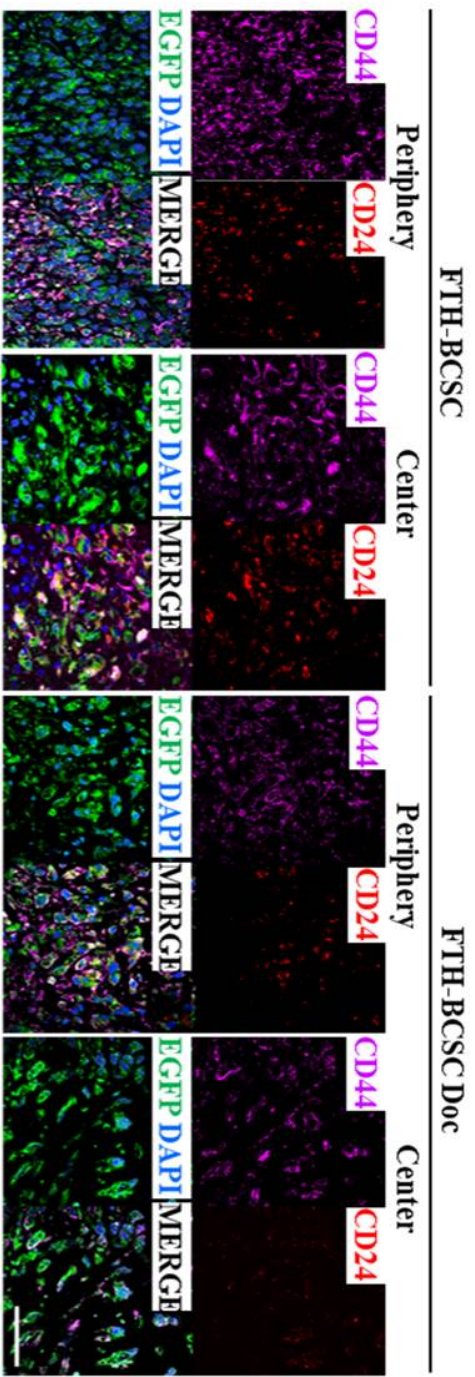


Figure 2–10. In vitro cytotoxicity test in BCSCs and FTH–BCSCs with docetaxel treatment.

(A) The percentages of JC–1 aggregates and cell viabilities after the docetaxel treatments were evaluated by the calculation of JC1 aggregates numbers on the fluorescence microscope images. (B–D) MTT assay and 7–AAD assay were performed to evaluate the toxicity of docetaxel in BCSCs and FTH–BCSCs.

A



B

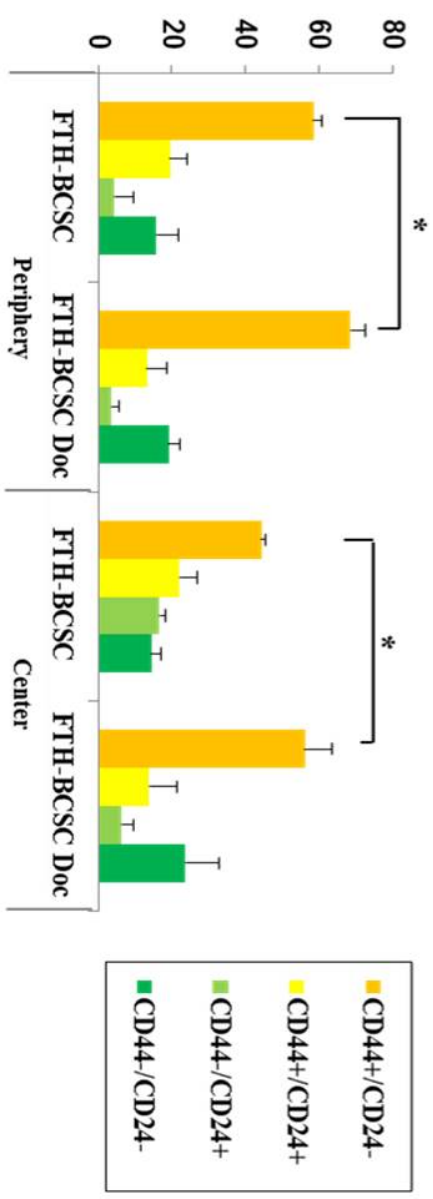


Figure 2–11. Immunohistochemical analysis of the peripheral and central portions of FTH–BCSC and docetaxel–treated FTH–BCSC Doc xenograft tumors.

(A) Double staining for CD44 and CD24 expression performed in FTH–BCSC and FTH–BCSC Doc tumors (x400; bar, 100 μ m). (B) The percentage of CD44+/CD24–, CD44+/CD24+, CD44–/CD24+, CD44–/CD24– and EGFP–positive cells in the periphery and center of the FTH–BCSC and FTH–BCSC Doc tumors. *P<0.05.

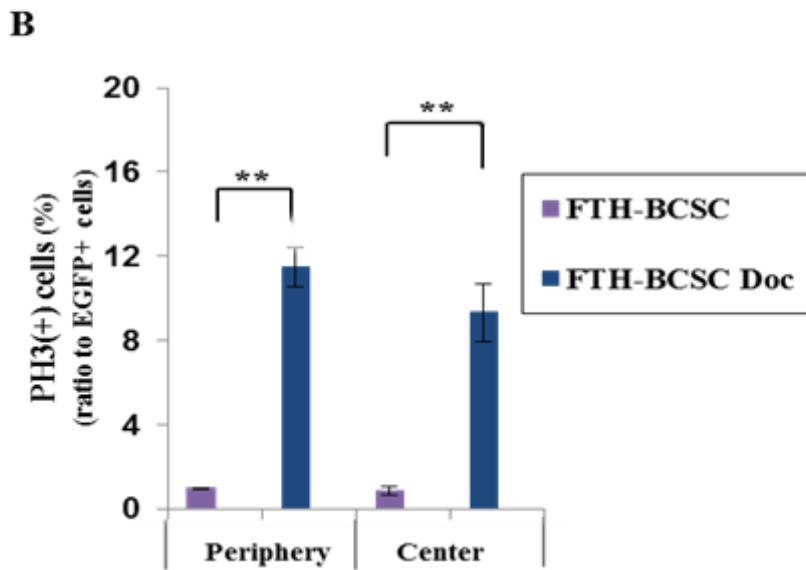
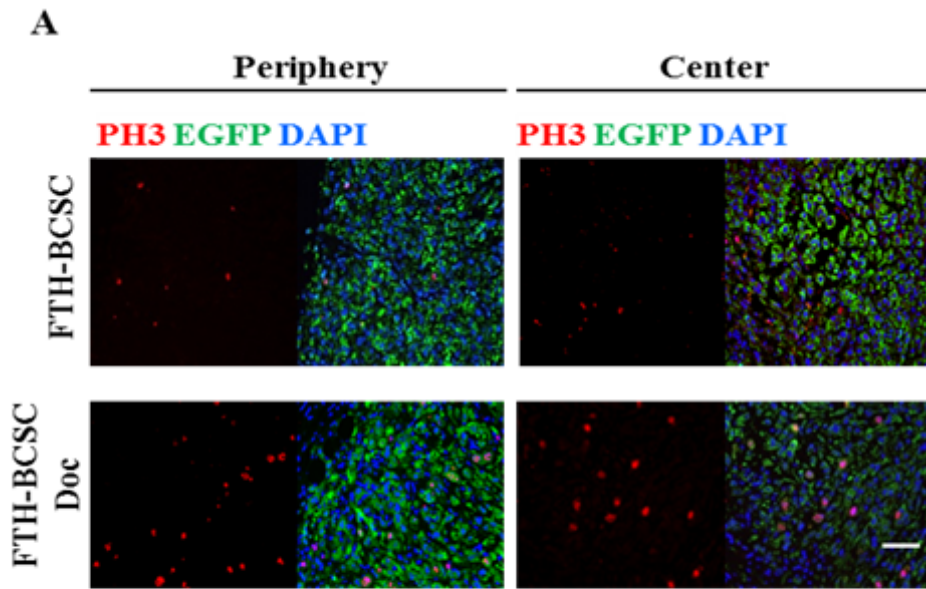


Figure 2–12. Analysis of tumor cell proliferation.

(A) Cell proliferation marker (phospho-histone 3, PH3) expression in the FTH-BCSC and FTH-BCSC Doc tumors (x200; bar, 100 μ m). (B) The percentage of PH3-positive/EGFP-positive cells in the periphery and center of the FTH-BCSC and FTH-BCSC Doc tumors. **P<0.01.

DISCUSSION

The results of this study suggest that ferritin-based MRI can be used as a noninvasive method to identify viable cell populations in tumors after chemotherapy. In the present study, BCSCs transduced with FTH and EGFP dual reporter genes were transplanted into NOD/SCID mice to noninvasively track BCSC-derived populations during tumor growth and monitor tumor responses after chemotherapy. MRI showed distinct populations of pixels with high R_2^* values in the docetaxel-treated FTH-BCSC tumors, which correspond to EGFP+ viable cell populations with a high percentage of CD44+/CD24- cells, as observed by histology. Results from this study confirmed that lentiviral transduction of the reporter genes did not alter the characteristics of BCSCs against the docetaxel, as were revealed by the cytotoxicity assays, and in vivo tumor growth. To the best of my knowledge, this study is the first to track –and image BCSCs isolated from human tumor specimens and to show viable cell populations of tumors after chemotherapy in living mice with MRI reporter genes. It is believed that this experimental model system can be used to identify the most effective treatments for tumors derived from BCSCs and to

develop new therapeutic strategies to target both BCSCs and non-BCSCs to achieve durable remission (8, 9, 18, 46).

A notable finding in this MRI study was the distinctive R_2^* value distribution found in FTH-BCSC tumors after chemotherapy. After 14 days of docetaxel treatment, a population of pixels with high R_2^* values appeared in the FTH-BCSC tumors while the mean R_2^* values of tumors were significantly decreased. In contrast, untreated BCSC, FTH-BCSC and docetaxel-treated BCSC tumors did not show this distinctive R_2^* value distribution. All R_2^* values for the control tumors showed a normal distribution. Pixels that represented a distinct population and measured over the threshold value (mean + 3SDs) of the docetaxel-treated FTH-BCSC tumors occupied approximately 50% of the total pixels, while the percentages for control tumors were under 30%. These findings support the result that cell populations with different R_2^* value distributions were distinguished by FTH overexpression. Finally, tissue analysis confirmed that the viable cells in the FTH-BCSC tumors after chemotherapy were only located in regions with high R_2^* values, while the viable cells in the BCSC tumors were in both regions with low and high R_2^* values. Together, these findings imply that MRI analysis using a ferritin reporter can identify and quantify

the existence of cells that survive after chemotherapy even before the tumor changes in size.

To monitor the BCSC tumor response to chemotherapy, this bimodal imaging approach based on FTH-EGFP dual reporter genes has advantages over optical imaging or MRI alone because areas of viable cells in tumors can be localized with 3D volumetric analysis of MRI data while the use of EGFP as a reporter gene enables the *in vitro* identification and molecular analysis of these viable cells (25, 27, 47, 48). Tissue samples from tumors could be obtained without sacrifice of animals by using an MRI-guided biopsy system (49). Furthermore, quantitative analyses of the MRI data enabled the evaluation of anti-tumor effects in different areas within the tumor, which is difficult with other *in vivo* methods. In this study, a higher percentage of cells with the CD44⁺/CD24⁻ phenotype was found in the remaining viable cells in the docetaxel-treated FTH-BCSC tumors than in the untreated FTH-BCSC tumors. This result demonstrates that more cells with the BCSC phenotype are present in docetaxel-treated tumors, which is consistent with results of previous studies (6). In the future clinical trials, the efficacy of BCSC-targeting therapies is likely be monitored *in vivo* with MRI and SPIO nanoparticle-labeling of anti-BCSC markers while our

imaging approach with bimodal reporter genes is more suitable for studying dynamic processes or tumor cells to stroma interaction in preclinical animal tumor models (46, 50–53).

In conclusion, this study results show that ferritin-based MRI, which offers high spatial resolution and tissue contrast, can effectively identify and localize remaining viable cell populations derived from BCSCs after chemotherapy and may represent a novel tool to monitor the efficacy of CSC-targeting therapies in vivo. The experimental model system used in this study could be easily applied to other cancer types, such as prostate, colon, pancreas, liver and brain tumors.

REFERENCES

1. Al-Hajj M, Wicha MS, Benito-Hernandez A, Morrison SJ, Clarke MF. Prospective identification of tumorigenic breast cancer cells. *Proceedings of the National Academy of Sciences of the United States of America*. 2003;100(7):3983–8. Epub 2003/03/12.
2. Dean M, Fojo T, Bates S. Tumour stem cells and drug resistance. *Nature reviews Cancer*. 2005;5(4):275–84. Epub 2005/04/02.
3. Phillips TM, McBride WH, Pajonk F. The response of CD24(–/low)/CD44+ breast cancer–initiating cells to radiation. *Journal of the National Cancer Institute*. 2006;98(24):1777–85. Epub 2006/12/21.
4. Yu F, Yao H, Zhu P, Zhang X, Pan Q, Gong C, et al. let-7 regulates self renewal and tumorigenicity of breast cancer cells. *Cell*. 2007;131(6):1109–23. Epub 2007/12/18.
5. Liu R, Wang X, Chen GY, Dalerba P, Gurney A, Hoey T, et al. The prognostic role of a gene signature from tumorigenic breast–cancer cells. *The New England journal of medicine*. 2007;356(3):217–26. Epub 2007/01/19.
6. Li X, Lewis MT, Huang J, Gutierrez C, Osborne CK, Wu MF, et al. Intrinsic resistance of tumorigenic breast cancer cells to chemotherapy. *Journal of the National Cancer Institute*. 2008;100(9):672–9. Epub 2008/05/01.
7. Wahl RL, Jacene H, Kasamon Y, Lodge MA. From RECIST to PERCIST: Evolving Considerations for PET response criteria in solid tumors. *Journal of nuclear medicine : official publication, Society of Nuclear Medicine*. 2009;50 Suppl 1:122S–50S. Epub 2009/06/24.
8. Hart LS, El-Deiry WS. Invincible, but not invisible: imaging approaches toward in vivo detection of cancer stem cells. *Journal of clinical oncology : official journal of the American Society of Clinical Oncology*. 2008;26(17):2901–10. Epub 2008/06/10.
9. Foster P. Imaging Cancer Stem Cells. In: Allan AL, editor. *Cancer Stem Cells In Solid Tumors*: Humana Press; 2011. p. 297–309.
10. Condeelis J, Weissleder R. In vivo imaging in cancer. *Cold Spring Harbor perspectives in biology*. 2010;2(12):a003848. Epub 2010/09/24.
11. Ignatius MS, Chen E, Elpek NM, Fuller AZ, Tenente IM, Clagg R, et al. In Vivo imaging of tumor–propagating cells, regional tumor heterogeneity, and dynamic cell movements in embryonal rhabdomyosarcoma. *Cancer cell*. 2012;21(5):680–93. Epub 2012/05/26.
12. Snyder EL, Bailey D, Shipitsin M, Polyak K, Loda M. Identification of CD44v6(+)/CD24– breast carcinoma cells in primary human tumors by quantum dot–conjugated antibodies. *Laboratory investigation; a journal of technical methods and pathology*. 2009;89(8):857–66. Epub 2009/06/03.
13. Vlashi E, Kim K, Lagadec C, Donna LD, McDonald JT, Eghbali M, et al. In vivo imaging, tracking, and targeting of cancer stem cells. *Journal of the National Cancer Institute*. 2009;101(5):350–9. Epub 2009/02/27.

14. Liu H, Patel MR, Prescher JA, Patsialou A, Qian D, Lin J, et al. Cancer stem cells from human breast tumors are involved in spontaneous metastases in orthotopic mouse models. *Proceedings of the National Academy of Sciences of the United States of America*. 2010;107(42):18115–20. Epub 2010/10/06.
15. Yoshii Y, Furukawa T, Kiyono Y, Watanabe R, Waki A, Mori T, et al. Copper-64-diacetyl-bis (N4-methylthiosemicarbazone) accumulates in rich regions of CD133+ highly tumorigenic cells in mouse colon carcinoma. *Nuclear medicine and biology*. 2010;37(4):395–404. Epub 2010/05/08.
16. Xia T, Jiang H, Li C, Tian M, Zhang H. Molecular imaging in tracking tumor stem-like cells. *Journal of biomedicine & biotechnology*. 2012;2012:420364. Epub 2012/05/10.
17. Shigdar S, Lin J, Li Y, Yang CJ, Wei M, Zhush Y, et al. Cancer stem cell targeting: the next generation of cancer therapy and molecular imaging. *Therapeutic delivery*. 2012;3(2):227–44. Epub 2012/07/28.
18. McLaughlin R, Hylton N. MRI in breast cancer therapy monitoring. *NMR in biomedicine*. 2011;24(6):712–20. Epub 2011/06/22.
19. Liu W, Frank JA. Detection and quantification of magnetically labeled cells by cellular MRI. *European journal of radiology*. 2009;70(2):258–64. Epub 2008/11/11.
20. Long CM, Bulte JW. In vivo tracking of cellular therapeutics using magnetic resonance imaging. *Expert opinion on biological therapy*. 2009;9(3):293–306. Epub 2009/02/17.
21. Artemov D, Mori N, Okollie B, Bhujwala ZM. MR molecular imaging of the Her-2/neu receptor in breast cancer cells using targeted iron oxide nanoparticles. *Magnetic resonance in medicine : official journal of the Society of Magnetic Resonance in Medicine / Society of Magnetic Resonance in Medicine*. 2003;49(3):403–8. Epub 2003/02/21.
22. Cohen B, Dafni H, Meir G, Harmelin A, Neeman M. Ferritin as an endogenous MRI reporter for noninvasive imaging of gene expression in C6 glioma tumors. *Neoplasia*. 2005;7(2):109–17. Epub 2005/04/02.
23. Genove G, DeMarco U, Xu H, Goins WF, Ahrens ET. A new transgene reporter for in vivo magnetic resonance imaging. *Nature medicine*. 2005;11(4):450–4. Epub 2005/03/22.
24. Gilad AA, Ziv K, McMahan MT, van Zijl PC, Neeman M, Bulte JW. MRI reporter genes. *Journal of nuclear medicine : official publication, Society of Nuclear Medicine*. 2008;49(12):1905–8. Epub 2008/11/11.
25. Kim HS, Cho HR, Choi SH, Woo JS, Moon WK. In vivo imaging of tumor transduced with bimodal lentiviral vector encoding human ferritin and green fluorescent protein on a 1.5T clinical magnetic resonance scanner. *Cancer research*. 2010;70(18):7315–24. Epub 2010/09/09.
26. Naumova AV, Reinecke H, Yarnykh V, Deem J, Yuan C, Murry CE. Ferritin overexpression for noninvasive magnetic resonance imaging-based tracking of stem cells transplanted into the heart. *Molecular imaging*. 2010;9(4):201–10. Epub 2010/07/21.

27. Townson JL, Ramadan SS, Simeanea C, Rutt BK, MacDonald IC, Foster PJ, et al. Three-dimensional imaging and quantification of both solitary cells and metastases in whole mouse liver by magnetic resonance imaging. *Cancer research*. 2009;69(21):8326–31. Epub 2009/10/22.
28. Choi SH, Cho HR, Kim HS, Kim YH, Kang KW, Kim H, et al. Imaging and quantification of metastatic melanoma cells in lymph nodes with a ferritin MR reporter in living mice. *NMR in biomedicine*. 2012;25(5):737–45. Epub 2011/11/30.
29. Theil EC. Ferritin: structure, gene regulation, and cellular function in animals, plants, and microorganisms. *Annual review of biochemistry*. 1987;56:289–315. Epub 1987/01/01.
30. Gottesfeld Z, Neeman M. Ferritin effect on the transverse relaxation of water: NMR microscopy at 9.4 T. *Magnetic resonance in medicine : official journal of the Society of Magnetic Resonance in Medicine / Society of Magnetic Resonance in Medicine*. 1996;35(4):514–20. Epub 1996/04/01.
31. Liu J, Cheng EC, Long RC, Yang SH, Wang L, Cheng PH, et al. Noninvasive monitoring of embryonic stem cells in vivo with MRI transgene reporter. *Tissue engineering Part C, Methods*. 2009;15(4):739–47. Epub 2009/03/18.
32. Ziv K, Meir G, Harmelin A, Shimoni E, Klein E, Neeman M. Ferritin as a reporter gene for MRI: chronic liver over expression of H-ferritin during dietary iron supplementation and aging. *NMR in biomedicine*. 2010;23(5):523–31. Epub 2010/02/23.
33. Eirew P, Stingl J, Raouf A, Turashvili G, Aparicio S, Emerman JT, et al. A method for quantifying normal human mammary epithelial stem cells with in vivo regenerative ability. *Nature medicine*. 2008;14(12):1384–9. Epub 2008/11/26.
34. Shipitsin M, Campbell LL, Argani P, Weremowicz S, Bloushtain-Qimron N, Yao J, et al. Molecular definition of breast tumor heterogeneity. *Cancer cell*. 2007;11(3):259–73. Epub 2007/03/14.
35. Horwitz KB, Dye WW, Harrell JC, Kabos P, Sartorius CA. Rare steroid receptor-negative basal-like tumorigenic cells in luminal subtype human breast cancer xenografts. *Proceedings of the National Academy of Sciences of the United States of America*. 2008;105(15):5774–9. Epub 2008/04/09.
36. Rennstam K, McMichael N, Berglund P, Honeth G, Hegardt C, Ryden L, et al. Numb protein expression correlates with a basal-like phenotype and cancer stem cell markers in primary breast cancer. *Breast cancer research and treatment*. 2010;122(2):315–24. Epub 2009/10/02.
37. Mani SA, Guo W, Liao MJ, Eaton EN, Ayyanan A, Zhou AY, et al. The epithelial-mesenchymal transition generates cells with properties of stem cells. *Cell*. 2008;133(4):704–15. Epub 2008/05/20.
38. Sarrío D, Rodríguez-Pinilla SM, Hardisson D, Cano A, Moreno-Bueno G, Palacios J. Epithelial-mesenchymal transition in breast cancer relates to the basal-like phenotype. *Cancer research*. 2008;68(4):989–97. Epub 2008/02/19.

39. Hogemann–Savellano D, Bos E, Blondet C, Sato F, Abe T, Josephson L, et al. The transferrin receptor: a potential molecular imaging marker for human cancer. *Neoplasia*. 2003;5(6):495–506. Epub 2004/02/18.
40. Liong M, Lu J, Kovochich M, Xia T, Ruehm SG, Nel AE, et al. Multifunctional inorganic nanoparticles for imaging, targeting, and drug delivery. *ACS nano*. 2008;2(5):889–96. Epub 2009/02/12.
41. McCarthy JR, Kelly KA, Sun EY, Weissleder R. Targeted delivery of multifunctional magnetic nanoparticles. *Nanomedicine (Lond)*. 2007;2(2):153–67. Epub 2007/08/25.
42. Islam T, Josephson L. Current state and future applications of active targeting in malignancies using superparamagnetic iron oxide nanoparticles. *Cancer biomarkers : section A of Disease markers*. 2009;5(2):99–107. Epub 2009/05/06.
43. Shah K, Jacobs A, Breakefield XO, Weissleder R. Molecular imaging of gene therapy for cancer. *Gene therapy*. 2004;11(15):1175–87. Epub 2004/05/14.
44. Massoud TF, Singh A, Gambhir SS. Noninvasive molecular neuroimaging using reporter genes: part II, experimental, current, and future applications. *AJNR American journal of neuroradiology*. 2008;29(3):409–18. Epub 2008/02/15.
45. Raty JK, Liimatainen T, Unelma Kaikkonen M, Grohn O, Airene KJ, Yla–Herttuala S. Non–invasive Imaging in Gene Therapy. *Molecular therapy : the journal of the American Society of Gene Therapy*. 2007;15(9):1579–86. Epub 2007/06/21.
46. Visvader JE, Lindeman GJ. Cancer stem cells: current status and evolving complexities. *Cell stem cell*. 2012;10(6):717–28. Epub 2012/06/19.
47. Medarova Z, Rashkovetsky L, Pantazopoulos P, Moore A. Multiparametric monitoring of tumor response to chemotherapy by noninvasive imaging. *Cancer research*. 2009;69(3):1182–9. Epub 2009/01/15.
48. Penet MF, Mikhaylova M, Li C, Krishnamachary B, Glunde K, Pathak AP, et al. Applications of molecular MRI and optical imaging in cancer. *Future medicinal chemistry*. 2010;2(6):975–88. Epub 2010/07/17.
49. Flegel T, Oevermann A, Oechtering G, Matiasek K. Diagnostic Yield and Adverse Effects of MRI–Guided Free–Hand Brain Biopsies through a Mini–Burr Hole in Dogs with Encephalitis. *Journal of veterinary internal medicine / American College of Veterinary Internal Medicine*. 2012. Epub 2012/06/20.
50. Hermann PC, Bhaskar S, Cioffi M, Heeschen C. Cancer stem cells in solid tumors. *Seminars in cancer biology*. 2010;20(2):77–84. Epub 2010/04/08.
51. Lim EK, Kim HO, Jang E, Park J, Lee K, Suh JS, et al. Hyaluronan–modified magnetic nanoclusters for detection of CD44–overexpressing breast cancer by MR imaging. *Biomaterials*. 2011;32(31):7941–50. Epub 2011/07/23.

52. Ross BD, Zhao YJ, Neal ER, Stegman LD, Ercolani M, Ben-Yoseph O, et al. Contributions of cell kill and posttreatment tumor growth rates to the repopulation of intracerebral 9L tumors after chemotherapy: an MRI study. *Proceedings of the National Academy of Sciences of the United States of America*. 1998;95(12):7012–7. Epub 1998/06/17.
53. Daldrup-Link HE, Golovko D, Ruffell B, Denardo DG, Castaneda R, Ansari C, et al. MRI of tumor-associated macrophages with clinically applicable iron oxide nanoparticles. *Clinical cancer research : an official journal of the American Association for Cancer Research*. 2011;17(17):5695–704. Epub 2011/07/28.

국문 초록

서론: 종양줄기세포는 종양의 형성과 성장 및 항암제 저항성의 원인으로 지목되고 있다. 종양 내 종양줄기세포 집단을 비침습적 영상법으로 가시화 하는 것은 종양줄기세포를 타겟으로 하는 치료법의 개발에 큰 영향을 줄 수 있을 것이다.

방법: 이 실험에서는 자기공명영상 리포터 유전자인 인간중쇄페리틴 (FTH)과 형광 리포터 유전자인 증강녹색형광단백질(EGFP)을 발현하는 유방암 줄기세포(BCSC)를 NOD/SCID 마우스에 이식하고 도세탁셀 치료 후 비침습적인 영상을 얻고 종양의 성장과 항암제에 대한 반응을 정량적으로 평가 하였다.

결과: 페리틴의 발현에도 BCSC의 생물학적 특성은 변하지 않은 것을 확인하였다. 자기공명영상에서 BCSC와 FTH-BCSC는 세포 수준과 종양 수준에서 유의하게 다른 신호강도(R_2^* 값)를 보였다. 도세탁셀을 투여한 FTH-BCSC 종양에서 대조군에 비해 R_2^* 값이 유의하게 다른 화소들을 발견하였고 조직 분석 결과 이 부위에 CD44+/CD24- 분획이 높은 EGFP+/FTH+ 생존 세포군을 확인하였다.

결론: 본 연구의 결과는 높은 공간 해상력과 조직 대조도를 제공하는 페리틴 기반 자기공명영상이 항암제 투여 후 생존하고 있는 BCSC 유래의 세포 군을 동정할 수 있으며 향후 BCSC 표적 치료제의 효능 평가에 새로운 도구로 사용될 수 있음을 시사한다.

주요어: 유방암 줄기세포, 페리틴, 항암치료, 리포터 유전자, 자기공명영상
학 번 : 2009-30615